TECHNICAL REPORT

HYPERSONIC TURBULENT BOUNDARY LAYER MEASUREMENTS USING AN ELECTRON BEAM

By: J. E. Wallace

CAL No. AN-2112-Y-1

Prepared for:

National Aeronautics and Space Administration
Environmental Factors and Aerodynamics Branch
Space Vehicles Division
Office of Advanced Research and Technology
Washington, D.C. 20546

FINAL REPORT

Contract No. NSR33-009-029
August 1968

CORNELL AERONAUTICAL LABORATORY, INC.
OF CORNELL UNIVERSITY, BUFFALO, N. Y. 14221

CORNELL AERONAUTICAL LABORATORY, INC.
BUFFALO, NEW YORK 14221

HYPERSONIC TURBULENT BOUNDARY LAYER MEASUREMENTS USING AN ELECTRON BEAM

FINAL REPORT

CAL REPORT NO. AN-2112-Y-1

CONTRACT NO. NSR33-009-029

AUGUST 1968

PREPARED FOR:

NATIONAL AERONAUTICS AND SPACE ADMINISTRATION
ENVIRONMENTAL FACTORS AND AERODYNAMICS BRANCH
SPACE VEHICLES DIVISION
OFFICE OF ADVANCED RESEARCH AND TECHNOLOGY
WASHINGTON, D.C. 20546

PREPARED BY: J. E. Wallace
J. E. Wallace

APPROVED BY: J. Gordon Hall
J. Gordon Hall, Head
Aerodynamic Research Department

FOREWORD

The research reported herein was sponsored by the National Aeronautics and Space Administration Headquarters under Contract NSR 33-009-029 and was monitored under the technical supervision of Mr. Fred DeMeritte of NASA Headquarters and of Mr. Ivan E. Beckwith of the NASA Langley Research Center. The work was performed by the Aerodynamic Research Department of the Cornell Aeronautical Laboratory, Inc. with the collaboration of the Hypersonic Facilities Department, Mr. R. Paul Mason and others, for the tests in the CAL 48-Inch Shock Tunnel. This technical report describes research performed during the period October 1966 to May 1968. The contractor's report number is AN-2112-Y-1.

ABSTRACT

Direct measurements of density and density fluctuations have been obtained in the cold-wall turbulent boundary layer on a shock-tunnel nozzle wall using an electron beam probe. Static temperatures and total enthalpy in the boundary layer inferred from the density measurements and accompanying pitot pressure measurements are found to be significantly below the values predicted by the Crocco energy relation. Measurements of skin friction and heat transfer on the nozzle wall are found to be in agreement with previous data obtained at higher Reynolds numbers.

TABLE OF CONTENTS

Section		Page
I.	INTRODUCTION	1
II.	TEST PROGRAM	3
	1. Test Configuration	3
	2. Instrumentation	3
	3. Test Conditions	5
III.	EXPERIMENTAL RESULTS	11
	1. Measured Boundary Layer Profiles	11
	2. Computed Boundary Layer Profiles	13
	3. Profile Integrations	16
	4. Wall Data	17
IV.	CONCLUSIONS	19
V.	REFERENCES	21
	APPENDIX - Electron Beam Density Probe	25
	1. Electron Beam Density Probe	25
	2. Equipment	27
	3. Beam Calibration	29
	4. Beam Profiles	31

LIST OF ILLUSTRATIONS

Figure		Page
1.	Nozzle Instrumentation for Turbulent Boundary Layer Experiments	35
2.	Nozzle Instrumentation and Viewing Optics	36
3.	Nozzle Pitot Pressure Distributions	37
4.	Experimental Data on the Nozzle Wall	38
5.	Photomultiplier Records from Electron Beam Luminescence in a Turbulent Boundary Layer	39
6.	Intensity of Density Fluctuations from Photomultiplier Records	40
7.	Records of Pitot Pressure in a Turbulent Boundary Layer	41
8.	Intensity of Pitot Pressure Fluctuations	42
9.	Measured Density Profiles	43
10.	Measured Pitot Pressure Profiles	44
11.	Comparison of Computed Experimental Velocity Profiles with Power Law Profiles	45
12.	Comparison of Experimental Temperature Profiles with Crocco Theory	46
13.	Comparison of Total Enthalpy Profiles with Crocco Theory	47
14.	Comparison of Turbulent Boundary Layer Skin Friction and Heat Transfer with Spalding and Chi Theory	48
15.	Electron Beam in Shock-Tunnel Nozzle Configuration	49
16.	Effect of Beam Spreading on Current Collection	50
17.	Density Calibration Curve	51
18.	Electron Beam Luminescence Profiles Calculated from Densitometer Readings of Beam Photograph	52
19.	Electron Beam Characteristics Determined from Densitometer Readings of Beam Photographs	53

LIST OF SYMBOLS

C_f	Local skin friction coefficient, $\tau_w / (\frac{1}{2} \rho_\infty u_\infty^2)$
D	Film density
E	Exposure
F_c	Spalding and Chi Factor, $F_c C_f = C_{f_i}$
F_{Rx}	Spalding and Chi Factor, $F_{Rx} Re_x = Re_{x_i}$
$F_{R\theta}$	Spalding and Chi Factor, $F_{R_\theta} Re_\theta = Re_{\theta_i}$
h	Static enthalpy
H	Total enthalpy
M	Mach number
n	Power law exponent
p	Pressure
p_s	Pitot pressure
$\dot{q}$	Heat transfer rate
r	Radial coordinate in nozzle; also recovery factor
Re	Reynolds number
St	Stanton number, $\dot{q} / \rho_\infty u_\infty (H_r - h_w)$
T	Temperature
u	Velocity
y	Coordinate normal to surface of nozzle wall
γ	Ratio of specific heats
δ	Boundary-layer thickness (based on pitot pressure profile)
δ_*	Boundary-layer displacement thickness
μ	Viscosity coefficient
ρ	Density
σ	Prandtl number
τ	Skin friction

SUBSCRIPTS

o	Reservoir conditions
AW	Adiabatic wall condition

LIST OF SYMBOLS (Cont.)

i	Incompressible, constant density case
r	Recovery
s	Stagnation point (behind normal shock on pitot probes)
w	Wall
∞	Freestream (in these experiments, conditions computed at the edge of the boundary layer from measured pitot pressure)

I. INTRODUCTION

Despite the considerable analytical and experimental work on compressible turbulent boundary layers which has been performed in recent years, a satisfactory and general description of turbulent flow is still lacking. The basic complexity of turbulent flow has led those seeking to describe the compressible case to hypothesize similarities between the compressible boundary layer and the constant density boundary layer, where at least a larger body of experimental measurements is available. Attempts to compare the theoretical work with compressible turbulent flow experiments have been limited by the lack of data at cold wall conditions (low values of h_w/H_o, or large heat transfer to the wall), by the lack of direct measurements of skin friction, and by incomplete experimental definition of the mean profiles and fluctuations across the boundary layer in high-speed compressible flows. Furthermore, the linear relation between total enthalpy and velocity required by the unit-Prandtl-number Crocco relation has often been assumed but not thoroughly checked for validity under the conditions of interest.

No attempt will be made here to review the numerous investigations of compressible turbulent flow which have been made in recent years; however, mention of some recent references for background is in order. The work by Spalding and Chi[1] included a rather comprehensive review of current theoretical methods as well as a new, semi-empirical theory. The transformation approach developed by Coles[2] has been modified by Crocco[3] and extended and applied by Baronti and Libby[4]. Extensions to compressible flow of Head's entrainment theory have been published by Standen[6] and Green[7], for example. Published results of direct skin friction measurements for turbulent flow include those reported by Neal[8] and Wallace[9].

Upon examination it will be found that all the theoretical and semi-empirical approaches rely, for a relation between static temperature (or density) and velocity in the boundary layer, upon the assumption of conservation of energy in the mean values of h and u and of the Crocco relation for unit Prandtl number, $\dfrac{H - h_w}{H_\infty - h_w} = \dfrac{u}{u_\infty}$, or a slight modification of it, e.g., replacement of the total enthalpy by an effective enthalpy ($H_r = h + r\frac{1}{2}u^2$ where r is a recovery factor) or by addition of a weak quadratic term in velocity. Discussions of these relationships are legion (Refs. 3, 10-14, for example), but direct measurements of enough boundary layer quantities to assess the relations assumed are relatively few (Refs. 15-19) and are limited to a range of h_w/H_e between 0.5 and 1.0 (adiabatic wall). With the exception of the data reported in Ref. 17 static temperatures inferred from measurements of total temperature and pitot pressure have been observed to agree with the Crocco relation only for the adiabatic wall case and have otherwise been found to be lower than predicted. This divergence appears, on the basis of the limited data available, to become greater with larger freestream Mach numbers and with decreasing values of h_w/H_e. Viewed in terms of the total enthalpy profile, the summary of experimental results reported by Bertram and Neal[20] indicates consistently lower values of total enthalpy in the turbulent boundary layer than either the unit-Prandtl-number Crocco relation or its modifications.

The objective of the present investigation has been to obtain a full complement of boundary layer measurements at low hypersonic, cold-wall conditions for a determination of the boundary layer profiles and their relationship to wall shear and heat transfer under these conditions. An electron beam luminescence probe has been used to measure the density in the turbulent boundary layer on a shock tunnel nozzle wall. In conjunction with measured pitot pressures in the boundary layer the density measurements have been used to compute the boundary layer profiles for the other thermodynamic and gasdynamic variables, in order to compare them with the Crocco relation. Simultaneous measurements of wall heat transfer and skin friction have also been made.

II. TEST PROGRAM

1. Test Configuration

The contoured expansion nozzle (nominal Mach number of 8) of the Cornell Aeronautical Laboratory 48-Inch Hypersonic Shock Tunnel[21] was instrumented to record skin friction, heat transfer, and pressure on the nozzle wall and to record pitot pressure and static density in the nozzle-wall boundary layer. A discussion of the design, operation and calibration of the electron beam is included in the Appendix. Figure 1 is a photograph of the instrumented nozzle wall in the vicinity of the station at which a 40 kV electron beam was projected through an orifice in the nozzle wall. A graphite cup, used to collect the beam current (approximately 1 milliampere), has been removed in the view shown to avoid obscuring the wall instrumentation. Hidden from view in Fig. 1 are the two stations instrumented with skin friction, pressure, and heat transfer gages upstream from the electron beam station. Figure 2 is a schematic drawing of the instrumentation arrangement and the optics for viewing the electron beam luminescence. The optics system, discussed further in the Appendix, was designed to obtain samples of the beam luminescence at 13 points over the boundary layer thicknesses of 5 to 6 inches. A set of miniaturized pitot probes was used to obtain pitot pressure data at 12 points within the boundary layer thickness.

2. Instrumentation

2.1. Pitot Probes

The boundary-layer pitot pressure transducers used in this program are described in Ref. 22. The basic transducer is 1/8-inch in diameter with an exposed diaphragm. Diaphragm deflections, in response to pressure forces, are mechanically transmitted to a cantilever beam of piezoceramic by means of a drive pin. To ensure dimensional stability of the transducer in the presence of temperature gradients, the diaphragm, the drive pin, the beam holder, and the case are fabricated from Invar, a material having a low coefficient of thermal expansion. The transducing beam consists of two layers of Sonotite 101 piezoceramic which are cemented together, oppositely poled, and series-connected electrically to achieve first order insensitivity to temperature. A second transducing beam (unattached to the diaphragm) provides an electrical signal that is used to achieve acceleration compensation. The entire force-sensing system, comprising the diaphragm, transducing beams, and holder constitutes a very small assembly which is placed at the probe tip where bending stresses are low. Nominally two inches long, the probe case is designed so that it may be extended to any desired length without disturbance to the force-sensing system or the electronic components. The probe incorporates a field-effect transistor and other necessary circuit elements to act as a cathode follower and preamplifier with a gain of approximately 2. Typical sensitivity is 50 mv/psi.

In the development of the pitot probe it was considered important to devise thermal protection for the diaphragm and crystal elements to avoid inducing false signals from temperature gradients in these materials. The best mode of protection developed was that of a labyrinth-path cap, consisting of an 0.035-inch diameter orifice in the outer cap, followed by a multiorifice plate, which in turn was followed by another 0.035-inch diameter orifice plate over the gage diaphragm. This configuration offered protection from convective heating, from radiative heating, and from possible damage by particles in the post-test flow. All but two of the twelve probes used in the present tests were of the labyrinth-path cap configuration. On the remaining two, the gage diaphragm was covered only by a thin layer (0.005 inch) of sheet rubber. The apparent adequacy of the thermal protection provided by this covering was attested by the good agreement between this configuration and the labyrinth-path cap configuration when all probes were placed in the uniform core flow of the nozzle. It was found that the dynamics of the signal fluctuations in the two types of probes do not differ significantly, i.e., the labyrinth-path cap does not seriously damp or mask the predominant oscillations in the flow impinging on the probe.

2.2 Wall Instrumentation

Skin friction gages developed at Cornell Aeronautical Laboratory for shock tunnel measurements[23] were used in the present program. A 1/4-inch diameter Invar sensing diaphragm is mounted flush with the instrumented surface and has a gap of approximately 0.010 inches around the diaphragm. The diaphragm is supported on two lead-zirconium-titanate crystals that are sensitive in a bending mode and insensitive in a compression mode. This provides the necessary sensitivity to tangential loading and insures a minimum response to normal loading. A third crystal is mounted within the case and loaded with a dummy mass to provide partial acceleration compensation. In the nozzle-wall application, where large accelerations of the wall are produced by the bursting of the shock tube diaphragm and by the reflection of the incident shock at the throat station, it was necessary to supplement the internal acceleration compensation of the gage by using the output of accelerometers mounted on the skin friction gage case to cancel the acceleration-induced signals in the skin friction gage. The matching of accelerometer output with that of the skin friction gage was accomplished on a shake table for three orthogonal axes. The base of the transducer contains a field effect transistor and other circuit elements that act as a cathode follower and preamplifier with a gain of approximately 2. Typically, the sensitivity for this instrument is 20 volts/psi.

Heat transfer and pressure instrumentation used in the present experiments was that now conventional for shock tunnel measurements. The heat transfer gages[24] were thin-film platinum strips on a pyrex substrate. Pressure gages[25] on the nozzle wall were shock isolated by mounting the transducer on a suspended mass and connecting the transducer with the orifice in the nozzle wall by a short length of flexible tubing. The response time of the pressure transducers, as well as that of the other transducers used, was comparable to the flow establishment time.

3. Test Conditions

A summary of the test conditions for the experimental program is provided as Table 1. Shock-tunnel reservoir enthalpy in the stagnated gas behind the reflected shock was computed for equilibrium air using the measured velocity of the incident shock. Reservoir pressure (behind the reflected shock) was measured directly. Free-stream conditions in the test section were

Table 1
TEST CONDITIONS

SYM.	$H_o(ft^2/sec^2)$	$T_o(°R)$	$p_o(psia)$	p_{s_∞} (psia)	M_∞	Re_∞/ft	$\rho_\infty(slugs/ft^3)$	$T_\infty(°R)$
○	2.43×10^7	3580	375	1.60	8.80	1.82×10^5	5.43×10^{-6}	245
△	2.41×10^7	3550	390	1.61	8.87	1.89×10^5	5.51×10^{-6}	240
⬭	2.40×10^7	3540	370	1.59	8.81	1.85×10^5	5.47×10^{-6}	240
▽	2.44×10^7	3590	385	1.61	8.82	1.84×10^5	5.45×10^{-6}	245
□	4.41×10^7	5815	845	3.35	8.22	1.54×10^5	6.22×10^{-6}	506
⌓	4.40×10^7	5805	845	3.30	8.25	1.52×10^5	6.13×10^{-6}	502
⬠	2.60×10^7	3795	240	1.10	8.62	1.10×10^5	3.48×10^{-6}	272
◇	1.92×10^7	2920	290	1.29	8.89	2.12×10^5	5.56×10^{-6}	189

$T_{WALL} = 525$ °R, $h_{WALL} = 3.16 \times 10^6$ ft^2/sec^2 IN ALL CASES calculated assuming an equilibrium air expansion to the measured test section pitot pressure. The narrow range in Reynolds number and total enthalpy encompassed by the test conditions is attributable to the lower limits on total enthalpy and reservoir pressure for which stable, fully developed nozzle flows are available and to the upper limits in density set by the onset of collision quenching of the electron beam-stimulated radiation and by spreading of the electron beam at the higher densities. The upper limit on density (2 Torr at room temperature or approximately 6 x 10^{-6} slugs/ft^3) was ultimately set by the requirement to protect the filament in the electron gun chamber from pressures above 10^{-5} Torr during calibration (see Appendix).

Precautions were taken to validate the choice of test conditions and of the configuration of the test hardware. The expansion nozzle consisted of a cylindrical throat of 0.964-inch diameter with a one-inch radius transition to a conical section with a 10.5-degree half angle, followed by a contoured wall. The wall contour is designed to cancel the expansion waves generated in the throat and conical section and to yield nearly parallel flow at the exit. Although the original nozzle had been cut off at 125 inches from the throat (with a wall angle of 0.76 degree at the exit), for the present experiments the original design contour was continued with a contoured extension for approximately three feet. The nozzle station at which the primary instrumentation was located was then 135 inches from the throat where the local wall angle is 0.58 degree. The additional extended nozzle length was provided to minimize end effects on the measurements. Because the nozzle had to be operated at local Mach numbers slightly in excess of the design Mach number of 8 in order to produce sufficiently low densities, the possibility of uncancelled waves reaching the test section had to be checked with measurements of pitot pressure in the inviscid core. The required uniform flow at the test station is attested by the shape of the radial profiles of pitot pressure shown in Fig. 3. The boundary-layer pitot pressure measurements, made after the nozzle calibration measurements, join smoothly with the profiles in the inviscid core. The results shown are representative of the four test conditions used in the program.

The correspondence between the present nozzle-wall boundary layer and that on a sharp flat plate may, of course, be influenced by the difference between the nozzle flow history and the uniform flow over a flat plate or by the small axial pressure gradient along the wall. However, any upstream disturbances of the boundary layer by wave systems would be expected to be rapidly diffused through the turbulent layer by turbulent mixing. In addition, good agreement in surface measurements has been found[9] in comparisons between sharp plate data and nozzle wall data obtained with the same nozzle as the present measurements, with the exception of the nozzle extension.

Wall pressures measured at three stations indicated a very small axial pressure gradient as shown in Fig. 4. The absence of any significant normal pressure gradients is indicated by a comparison of these values of measured static pressure at the wall with the free-stream static pressure computed from measured pitot pressure (Fig. 4), which reveals good agreement between the measured and computed static pressures and which also suggests that the nozzle expansion is isentropic (free of shocks). For reference purposes, Fig. 4 also includes the values of skin friction and heat transfer measured on the nozzle wall.

The assurance that the boundary-layer flow was turbulent in the instrumented region of the nozzle wall lies in the boundary layer profiles and the wall measurements themselves. However, it can be noted that in a shock tunnel test program with reservoir conditions comparable to the present ones, Burke[26] found that the throat Reynolds numbers were high enough to achieve transition to turbulent flow in the throat region. Furthermore, the Reynolds numbers based on local conditions and nozzle length were relatively high -- in the range of 1×10^6 to 3×10^6.

Several possible types of interference were evaluated. Possible interference between the pitot probes and the wall instrumentation was assessed by operating the shock tunnel at a given condition with and without the pitot probe rake in position. No perceptible difference in measured pressure, heat transfer, or skin friction was observed. Possible wall interference with the pitot probe measurement closest to the wall was minimized by placing the lower edge of that probe just above the subsonic portion of the boundary layer.

The possibility of disturbances in the wall measurements from the viewing-optics port was explored by making identical shock tunnel runs with the viewing-optics port open and with it closed by a cover contoured to the nozzle wall geometry. No differences in wall data were observed.

Finally, a check was made of the background radiation by recording the light received by the photomultiplier during a shock tunnel run with the electron beam turned off. The received light was completely negligible compared with the light levels recorded during runs with the electron beam on.

III. EXPERIMENTAL RESULTS

1. Measured Boundary Layer Profiles

Typical shock tunnel records of the density measurements obtained in the nozzle-wall boundary layer are shown in Fig. 5. The oscilloscope pictures of the beam fluorescence are of particular interest because of the details revealed in the signal dynamics. The magnitude of the fluctuations in the photomultiplier output is seen to vary from very small fluctuations near the wall to large fluctuations in the interior of the boundary layer and back to very small fluctuations as the free-stream core flow is approached. The consistent variation in the relative amplitude of the fluctuations and the degree of correlation of the details of the signal dynamics for adjacent points along the beam suggest that the fluctuations seen are real variations in the local light intensity; hence, these fluctuations presumably represent real variations in density within the gas volume viewed by the optics systems (see Appendix). This feature of the records suggests that detailed measurements of the turbulence-induced fluctuations would be feasible and could yield information on the turbulence structure in compressible turbulent boundary layers.

For present purposes a simple analysis of the oscilloscope records has been made to determine the root-mean-square value of the fluctuations from the mean density level during the first four milliseconds of quasi-steady flow.* In view of the small degree of nonlinearity in the relationship between the photomultiplier output and the gas density (see Appendix), the fluctuations in the photomultiplier signal are taken to represent density fluctuations. Barred symbols will be used to indicate average values; symbols

---

* The digitizing of the analog data and computing of the RMS values of the fluctuations were performed at the NASA Langley Research Center under the supervision of Messrs. Ivan E. Beckwith and William D. Harvey. Each analog record was digitized at 100 points per millisecond of record over a period of four milliseconds.

with a prime will be used to indicate the flucutuating component. Figure 6 is a summary plot of the variation across the boundary layer in the intensity of density fluctuations, defined as the ratio of the root-mean-square of the fluctuations to the local mean value, $\left(\overline{\rho'^2}\right)^{1/2}/\bar{\rho}$. The peak fluctuation intensity occurs near the wall $(y/\delta \cong 0.05)$, as had been previously inferred in other investigations of turbulent boundary layers[27, 28], but without direct measurements of density. A curious phenomenon is observed in the present data, however, in the form of an inflection at approximately $0.2 < y/\delta < 0.5$ in the curve of fluctuation intensities. This behavior would doubtless have been attributed to random scatter and brushed aside had it not been for a similar occurrence in the variation of both the density and the pitot pressure fluctuation intensities.

Samples of the pitot pressure records are included in Fig. 7. These indicate that the pitot-pressure fluctuations are much larger in relative magnitude than the density fluctuations. (The apparent "stepped" character of the pitot pressure records is caused by the data recording system used to obtain the pitot data. This system samples a given signal every 50 microseconds, stores it on a drum during the run, and after the run displays the signal on a strip-chart recorder.) Once again it is observed that the largest fluctuations occur in the boundary layer relatively close to the wall and diminish toward the edge of the boundary layer. However, the inflection point is again observed when the RMS value of the fluctuations from the mean in pitot pressure is computed and plotted against boundary layer position as in Fig. 8. Whether this phenomenon is, in fact, a general characteristic of compressible turbulent boundary layers at cold wall conditions remains for further investigation.

In Fig. 9 the mean values of density inferred from the electron beam measurements are presented. Densities in the interior of the boundary layer are normalized by the values at the edge of the boundary layer. Edge values of density were obtained by extrapolation to the boundary-layer edge obtained from the pitot pressure profiles. (The determination of the location of the boundary layer edge was based on subjectively identifying the point on the pitot pressure profiles at which the freestream pitot pressure was reached.

Simultaneous changes in Mach number, Reynolds number and total temperature produced approximately the same thickness, 5.9 inches, for the last two test conditions.) Points shown at the wall represent the wall density as computed from the freestream static pressure and the pre-run wall temperature (nominally 525 °K). Test durations are so short that there is no significant rise in the nozzle wall temperature during the test period. Data points for the first condition shown represent the average of data from two shock tunnel runs.

Because of apparently spurious records, three of the photomultiplier channels were discarded. The remaining data scatter was such that a point-to-point following of the data did not seem realistic; consequently, the smooth curves shown faired through the data in Fig. 9 were used in the further calculations of boundary layer profiles. A more exact following of the density data points would not alter the qualitative observations made later with regard to temperature and velocity profiles. It is noted, however, that there is a possible inflection in the mean density profiles in the same region of the boundary layer at which inflections are observed in the profiles of the fluctuation intensity for both density and pitot pressure.

Pitot pressure profiles are presented in Fig. 10. The plotted points represent averages from four runs at the first test condition and from two runs at the third test condition. The free-stream static pressure was used to obtain points at the wall. The present nozzle boundary-layer profiles are seen to be qualitatively similar to profiles obtained[19] on an entirely different geometry -- a hollow cylinder.

2. Computed Boundary Layer Profiles

Using the measured density and pitot pressure results, profiles of temperature, velocity and total enthalpy have been computed and are presented in Figs. 11, 12 and 13. Since the measured wall static pressure is in good agreement with the free-stream static pressure computed from measured pitot pressure, the assumption of constant pressure across the boundary layer is justified. For an ideal gas the equation of state then yields $T/T_\infty = \rho_\infty/\rho$, where the density ratio is taken from the faired curves in Fig. 9.

The velocity ratio, u/u_∞, is obtained by using the measured pitot pressure and density profiles. Denoting conditions at the stagnation point on the pitot probe by subscript, "s", conditions behind the standing normal shock by subscript "1" (all probes were in the supersonic portion of the boundary layer), and conditions ahead of the normal shock with no subscript, the normal shock relations

$$\frac{p_1}{p} = 1 + \frac{2\gamma(M^2-1)}{\gamma+1} \tag{1}$$

and

$$\frac{\rho}{\rho_1} = \frac{\gamma-1}{\gamma+1} + \frac{2}{(\gamma+1)M^2} = \frac{u_1}{u} \tag{2}$$

are substituted in the incompressible-flow Bernoulli equation for the subsonic region behind the shock

$$p_s = p_1 + \frac{1}{2}\rho_1 u_1^2 \tag{3}$$

to obtain

$$\left(\frac{u}{u_\infty}\right)^2 = \frac{p_s}{p_{s_\infty}} \frac{\rho_\infty}{\rho} \frac{1 - \frac{1}{2}\frac{\gamma-1}{\gamma+1} + \frac{1}{\gamma(\gamma+1)M_\infty^2}}{1 - \frac{1}{2}\frac{\gamma-1}{\gamma+1} + \frac{1}{\gamma(\gamma+1)M^2}} \tag{4}$$

The term with local Mach number in this expression is a small correction except for the low supersonic region. Values for local Mach number were first obtained from the ideal gas NACA tables[29] as a function of p_∞/p_s in the boundary layer, then revised from $M/M_\infty = (u/u_\infty)(T/T_\infty)^{1/2}$ in cases near the wall where iteration was necessary. The resulting velocity profiles are presented in Fig. 11. For purposes of comparison, power law profiles of $u/u_\infty = (y/\delta)^n$ are shown. Turbulent boundary-layer velocity profiles are usually associated with small values of n, typically n = 1/7 to 1/10. However, it is clear that the present results agree best with larger values of n, typically n = 1/3. It should be noted that more conventional velocity profiles result if, as shown in Fig. 11 for the 1.85 x 10^5/ft unit Reynolds number case, the measured density is ignored and the velocity profile computed from the measured pitot pressure and the Crocco energy relation $\frac{u}{u_\infty} = \frac{H-h_w}{H_\infty - h_w}$. This approach was necessary in previous studies[9] of turbulent boundary layers at higher Reynolds numbers, when pitot pressure was the only variable measured directly. The results of such a computation are shown only for one test condition; but the resulting profile does indicate that the boundary layer under study would be adjudged typically turbulent in view of its favorable comparison with the 1/10th power law profile.

A presentation of the static temperature ratio, T/T_∞, (inverse of density ratio) versus computed velocity in Fig. 12 clearly indicates the divergence of the present measurements from the temperature profile predicted by the Crocco relation (in conjunction with the energy equation)

$$\frac{T}{T_\infty} = \frac{T_w}{T_\infty} + \left(\frac{H_\infty}{h_\infty} - \frac{T_w}{T_\infty}\right)\frac{u}{u_\infty} - \left(\frac{H_\infty}{h_\infty} - 1\right)\left(\frac{u}{u_\infty}\right)^2 \quad (5)$$

Profiles of total enthalpy as a function of velocity are presented in Fig. 13. These further illustrate the divergence from the Crocco relation. The cross-hatched area on Fig. 13 represents a summary[20] of previous data obtained from experimental pitot pressure and total temperature measurements, which are substantially in agreement with the present results. Purely as an empiricism, a curve for $\frac{H-h_w}{H_\infty - h_w} = \left(\frac{u}{u_\infty}\right)^2$ is drawn in Fig. 13 and is seen to describe much more adequately the experimental results than the classical, linear Crocco relation. Other more rational, but less successful, modifications of the Crocco relation are discussed in Ref. 9. It is noted in both Fig. 12 and Fig. 13 that, within the limited range of unit Reynolds numbers developed, the divergence of the experimental results from the Crocco theory appears to increase with increasing Reynolds number. However, the same trend is observed with higher ratios of h_w/H_∞, despite the fact that in the adiabatic wall case ($h_w/H_\infty = 1$) agreement with the Crocco relation is known to be good. The apparent trends with Reynolds number and wall cooling may thus be within the experimental error.

3. Profile Integrations

Appropriate integrations have been performed to obtain the usual boundary-layer profile parameters, displacement thickness and momentum thickness. The axisymmetric forms of the expressions for displacement and momentum thicknesses[9] have been used, because the boundary layer thickness is roughly half the nozzle radius. Density and velocity values from the experimental data have been substituted in

$$\frac{\delta_*}{\delta} = \frac{1 - \left\{1 - 2\frac{\delta}{r_w}\left[1 - \frac{\delta}{2r_w} - \int_0^{\delta} \frac{\rho u}{\rho_\infty u_\infty}\left(1 - \frac{y}{r_w}\right) dy\right]\right\}^{1/2}}{\delta / r_w} \tag{6}$$

and

$$\frac{\theta}{\delta} = \frac{1 - \left[1 - 2\frac{\delta}{r_w}\int_0^{\delta} \frac{\rho u}{\rho_\infty u_\infty}\left(1 - \frac{u}{u_\infty}\right)\left(1 - \frac{y}{r_w}\right) dy\right]^{1/2}}{\delta / r_w} \tag{7}$$

where r_w denotes the local radius (11.63 inches) of the nozzle. For purposes of comparison with results based only on pitot pressure data, the first case has also been computed using the velocity and density obtained from the measured pitot pressure plus the Crocco relation. These results are shown in parentheses and are found to compare favorably with previous data[9]. The complete results from the present experiments are tabulated in Table 2. Values have been grouped for the repeat conditions listed in the test conditions, Table 1.

Table 2

BOUNDARY LAYER THICKNESS

T_0(°R)	M_∞	Re_∞/ft	δ_*/δ	θ/δ	δ_*/θ
3560	8.82	1.85×10^5	0.335(0.279)	0.0778(0.0213)	4.305(13.1)
5810	8.24	1.53×10^5	0.319	0.0890	3.59
3790	8.62	1.10×10^5	0.357	0.0688	5.19
2920	8.89	$2,12 \times 10^5$	0.329	0.0873	3.77

The only further use made of these results in the present work is in the comparison of measured values of skin friction with shear laws based on momentum thickness Reynolds numbers.

4. Wall Data

In the present results the measurements of heat transfer and skin friction on the wall are used primarily as a verification that the nozzle boundary layer is turbulent. On the basis of its successful application in the author's previous studies[9] the compressible turbulent boundary layer theory of Spalding and Chi[1] has been relied upon for purposes of comparison. It should be noted, however, that in the development of the Spalding and Chi theory the mixing-length related parameter, F_c, was computed using a slightly modified Crocco relation, as noted in Ref. 9. It has been shown that the experimental results differ significantly from the Crocco relation. When the Spalding and Chi theory is applied to the present heat transfer and skin friction data, the resulting comparison, as shown in Fig. 14, yields results comparable to those reported previously[9] for higher unit Reynolds number flows with the same basic experimental set-up as the present one (excepting the nozzle extension). (Two heat transfer curves are shown - one for the unit Prandtl number Reynolds analogy, $2St = C_f$, and one for the Colburn modification of Reynolds analogy, $2St = \sigma^{-2/3} C_f$.) Thus, despite the low unit Reynolds numbers required in the present experiments to remain within the operating range of the electron beam, the flow is still a turbulent one.

For the case in which the Crocco relation was used in conjunction with measured pitot pressures to obtain profiles for the momentum thickness integration, the resulting momentum thickness Reynolds number was used to compare the experimental value of the skin friction coefficient with Spalding and Chi theory. The resulting data point is less than ten per cent above the Spalding and Chi theory, as had been the case for the nozzle measurements reported previously[9]. This comparison is consistent with the way in which Spalding and Chi developed their theory. However, when the density profiles from the present experiments are used to calculate the value of the coefficient for C_f,

$$F_c = \left[\int_0^1 \left(\frac{\rho}{\rho_\infty} \right)^{1/2} d\frac{u}{u_\infty} \right]^{-2}$$

the value for F_c becomes 1.72 compared to the Spalding and Chi value of 3.62. Since the F_c value is involved in the Spalding and Chi error minimization used in choosing the momentum thickness Reynolds number coefficient, F_{R_θ}, it is not possible to locate within the Spalding and Chi results a value of F_{R_θ} consistent with the values of F_c and R_θ taken directly from the present experiments. Thus, as a prediction method the Spalding and Chi formulation is internally consistent and provides consistently good predictions. But as an actual description of the relationship between compressible, cold-wall turbulent boundary layers and the constant density turbulent boundary layer, the Spalding and Chi formulation fails to incorporate the apparent discrepancies observed here between the Crocco relation and measurements obtained at cold wall conditions.

IV. CONCLUSIONS

It has been demonstrated in a series of measurements with an electron beam probe in the boundary layer of a shock-tunnel nozzle wall that direct measurements of densities and density fluctuations can be obtained in a turbulent boundary layer. Both the density measurements and accompanying pitot pressure measurements indicate peak fluctuation intensities quite near the wall.

The direct measurement of boundary layer density in the present experiments, in conjunction with measured pitot pressures, has confirmed the substantial deviation from the simple Crocco energy relation of actual turbulent hypersonic turbulent boundary layers at cold wall conditions. The degree of deviation in temperature and total enthalpy from the Crocco relation has marked effects upon the integrated boundary layer thicknesses. As a result the attempted comparison with the Spalding and Chi theory failed, except when the Crocco relation was invoked instead of using the measured density.

V. REFERENCES

1. Spalding, D.B. and Chi, S.W., "The Drag of a Compressible Turbulent Boundary Layer on a Smooth Flat Plate with and without Heat Transfer," Journal of Fluid Mechanics, Vol. 18, Part I, 1964, pp. 117-143.

2. Coles, D.E., "The Turbulent Boundary Layer in a Compressible Fluid," RAND Corp. Rept. R-403-PR, September 1962.

3. Crocco, L., "Transformation of the Compressible Turbulent Boundary Layer with Heat Exchange," AIAA Journal, Vol. 1, No. 12, December 1963, pp. 2723-2731.

4. Baronti, P.O. and Libby, P.A., "Velocity Profiles in Turbulent Compressible Boundary Layers," AIAA Journal, Vol. 4, No. 2, February 1966, pp. 193-202.

5. Head, M.R., "Entrainment in the Turbulent Boundary Layer," Aeronautical Research Council (G.B.) R&M 3152, 1958.

6. Standen, N.M., "A Concept of Mass Entrainment Applied to Compressible Turbulent Boundary Layers in Adverse Pressure Gradients," AIAA Paper No. 64-584, 1964.

7. Green, J.E., "The Prediction of Turbulent Boundary Layer Development in Compressible Flow," Journal of Fluid Mechanics, Vol. 34, Part 4, 1968, pp. 753-778

8. Neal, Luther, Jr., "Pressure Heat Transfer and Skin Friction Distributions over a Flat Plate Having Various Degrees of Leading Edge Bluntness at a Mach Number of 6.8," NASA TN D-3312, April 1966.

9. Wallace, J.E., "Hypersonic Turbulent Boundary-Layer Studies at Cold Wall Conditions," Proceedings of the 1967 Heat Transfer and Fluid Mechanics Institute, Paul A. Libby, et al., editors, Stanford University Press, 1967, pp. 427-451.

10. Cohen, N.B., "A Method for Computing Turbulent Heat Transfer in the Presence of a Streamwise Pressure Gradient for Bodies in High-Speed Flow," NASA Memo I-2-59L, March 1959.

11. Spence, D.A., "Some Applications of Crocco's Integral for the Turbulent Boundary Layer," Proceedings of the 1960 Heat Transfer and Fluid Mechanics Institute, D.M. Mason et al., editors, Stanford University Press, 1960, pp. 62-76.

12. Kutateladze, S.S. and Leont'ev, A.I. (Translated by D.B. Spalding), Turbulent Boundary Layers in a Compressible Gas, New York: Academic Press, 1964, pp. 25-29.

13. Walz, A. "Compressible Turbulent Boundary Layers," in The Mechanics of Turbulence, New York: Gordon and Breach Science Publishers, Inc., 1964 (Proceedings of Colloque International Sur," La Mechanique de la Turbulence," Marseille, August 28 to September 2, 1961), pp. 299-350.

14. Rotta, J.C., "Heat Transfer and Temperature Distributions in Turbulent Boundary Layers at Supersonic and Hypersonic Flow," in "Recent Developments in Boundary Layer Research," AGARDograph 97, Part I, May 1965, pp. 35-63.

15. Lobb, R.K., Winkler, E.M. and Persh, S., "Experimental Investigation of Turbulent Boundary Layers in Hypersonic Flows," Journal of Aeronautical Sciences, Vol. 22, No. 1, 1955, pp. 1-9, 50.

16. Hill, F.K., "Turbulent Boundary Layer Measurements at Mach Numbers of 8 to 10," Physics of Fluids, Vol 2, 1959, pp. 668-680.

17. Winkler, E.M. and Cha, M., "Investigation of Flat Plate Hypersonic Turbulent Boundary Layers with Heat Transfer at a Mach Number of 5.2," NAVORD Rept. 6631, 1959, U.S. Naval Ordnance Lab., White Oak, Md.

18. Danberg, J.E., "Characteristics of the Turbulent Boundary Layer with Heat and Mass Transfer at M = 6.7," NOLTR 64-99, October 1964, Naval Ordnance Lab., White Oak, Md.

19. Samuels, R.D., Peterson, J.B., Jr. and Adcock, J.B., "Experimental Investigation of the Turbulent Boundary Layer at a Mach Number of 6 with Heat Transfer at High Reynolds Numbers," NASA TN D-3858, March 1967.

20. Bertram, M.H. and Neal, L., Jr., "Recent Experiments in Hypersonic Turbulent Boundary Layers," NASA TMX-56335, May 1965.

21. "Cornell Aeronautical Laboratory Hypersonic Shock Tunnel, Description and Capabilities," April 1968, Cornell Aeronautical Lab., Buffalo, N.Y.

22. MacArthur, R.C., "The Development of High Output Pressure Transducers for Shock Tunnel Testing," Rept. TR-68-37, April 1968, Air Force Aero Propulsion Laboratory, (Cornell Aeronautical Lab., Buffalo, N.Y.).

23. MacArthur, R. C., "Contoured Skin Friction Transducer," Rept. AN-2403-Y-1, August 1967, Cornell Aeronautical Lab., Buffalo, N. Y.

24. Vidal, R.J., "Transient Surface Temperature Measurements," Rept. 114, March 1962, Cornell Aeronautical Lab., Buffalo, N.Y.

25. Martin, J.F., Duryea, G.R. and Stevenson, L.M., "Instrumentation for Force and Pressure Measurements in a Hypersonic Shock Tunnel," Advances in Hypervelocity Techniques, Plenum Press, 1962, (Cornell Aeronautical Laboratory Rept. No. 113).

26. Burke, A. F., "Turbulent Boundary Layers on Highly Cooled Surfaces at High Mach Numbers," in Symposium on Aerothermoelasticity, Dayton, Ohio, October 3 to November 1, 1961, Air Force Aeronautical Systems Div., TR 61-645, pp. 704-741.

27. Kistler, A. L., "Fluctuation Measurements in a Supersonic Turbulent Boundary Layer," Physics of Fluids, Vol. 2, No. 3, 1959, pp. 290-296.

28. Morkovin, M. V., "Effects of Compressibility on Turbulent Flows," in The Mechanics of Turbulence, New York: Gordon and Breach Science Publishers, Inc., 1964, pp. 367-380.

29. "Equations, Tables, and Charts for Compressible Flow," NACA Rept. 1135.

30. Llinas, J. and Rustay, W. C., "Temperature and Density Measurements in the Base Region of a Clustered Rocket Model Using an Electron-Beam Technique," Rept. HM-2107-Y-1, July 1966, Cornell Aeronautical Lab., Buffalo, N. Y.

31. Muntz, R. P., Abel, S. J. and Maguire, B. L., "The Electron Beam Fluorescence Probe in Experimental Gas Dynamics," Supplement to IEEE Transactions on Aerospace, Vol. AS-3, No. 2, June 1965, pp. 210-222.

32. Davidson, G. and O'Neil, R., "The Fluorescence of Air and Nitrogen Excited by 50 keV Electrons," Rept. AFCRL-64-466, May 1964, Air Force Cambridge Research Labs. (also American Science and Engineering, Inc. Rept. ASE-512 and DDC No. AD 608058).

33. Camac, M., "Boundary Layer Measurements with an Electron Beam," Research Rept. 275, July 1967, AVCO Corp., Everett Research Lab., Everett, Mass. (prepared for Bell Telephone Labs., Inc.).

APPENDIX

ELECTRON-BEAM DENSITY PROBE

1. Electron-Beam Density Probe

The electron-beam density-probe technique is based on the stimulation of emission from a gas by collisional excitation using a beam of energetic electrons (energies usually greater than 10 kV). Inelastic collisions between the gaseous molecules and the beam electrons result in the production of electronically excited molecules or molecular ions and the subsequent radiative transition to the electronic ground state of the molecule or ion, which produces a gaseous fluorescence coincident with the electron beam. If the radiative transition is unaffected by gas-kinetic collisions, the local emitted intensity is directly proportional to the local gas number density of molecules (such other conditions as beam current and beam voltage held constant). With the fluorescent light yield detected at a number of points along the beam with photomultipliers and with the beam continuously in operation during the test event, spatially and temporally resolved measurements can be made.

To achieve a luminescence which is linear with the number density of molecules, one desires that the particular emission to be used result from a direct excitation-emission sequence and that the excited state involved in the transition be reached by direct excitation from the ground state of the neutral molecule. In the case of nitrogen, which has been studied extensively in the application of the electron beam probe to number density and temperature measurements in gas flows, the most prominent system excited is the first negative system of N^+_2 with spectral emission located approximately in the 3800 Å to 4300 Å band. Investigations have been conducted at Cornell Aeronautical Laboratory using both nitrogen and air.[30] The present study used air exclusively as the test gas. The mean lifetime of the excited state of N^+_2 is only about 6×10^{-8} sec., so that the extent to which the flow carries radiating molecules away from the region viewed (that is, the region of initial excitation by the beam) is negligibly small. The spatial resolution is limited only by the beam diameter and length of beam selected for observation.

In addition to the inelastic collisions, elastic collisions between molecules and beam electrons can occur; these elastic collisions contribute primarily to scattering of the electron beam which causes a spreading of the light emanating from the region of the beam (See Figure 15). Scattering increases with number density and causes a loss of spatial resolution in density measurements, since it is necessary to observe the total emission. A measure of control over scattering is possible by increasing the beam accelerating voltage, since electron-neutral collision cross sections decrease with increasing electron energy. However, a reduction in emission intensity (for a given beam current) also occurs due to the concurrent reduction in the number of inelastic collisions. Muntz[31] has pointed out that the improvements resulting from the use of beam energies exceeding 50 kV to counteract beam spreading are small, especially in view of the rapidly increasing cost and complexity of operating equipment above that voltage level and the increased radiation (X-ray) hazards to operating personnel. The present beam was operated at 40 kV.

The measurement of molecular number density is conceptually simple. Emission intensity is measured from the full width and some arbitrary length of the beam together with a simultaneous measurement of beam current. Since emission intensity is a directly proportional to beam current, accurate measurement of current is of fundamental importance, and corrections for any variation in beam current during the test interval are necessary. In addition, the sensing optics must accommodate the full beam width; this consideration is especially important if accurate density measurements are to be obtained in the presence of appreciable beam spreading. The length of beam observed will generally be determined a compromise between need to achieve satisfactory signal-to-noise ratios in the optical sensors at low densities and the requirements of spatial resolution.

For nitrogen densities equivalent to room temperature pressures of less than about 500 microns Hg, emission intensity is directly proportional to number density. With increasing density, collisional de-excitation (quenching) becomes important and the linear relation between density and emission intensity is lost, as is ultimately the sensitivity of emission intensity to changes in density.

2. Equipment

For a schematic drawing of the electron beam installation used in the present program, reference is again made to Figure 2. The 40 kV electron beam was projected through the nozzle wall and collected in a graphite cup. The electron gun is an air-cooled, grid-controlled, electrostatically focused RCA J1694 unit with a directly heated tungsten cathode. The electron gun control unit and power supply is an RCA VX2207 unit. The electron beam is projected through a series of orifices (apertures) to generate a collimated beam of electrons. The orifices serve both to collimate the beam and to isolate the beam generating apparatus into a series of chambers that are differentially pumped to provide the necessary pressure buffering between the high vacuum required for the electron gun and the higher pressure of the shock tunnel test section.

The upper limit in density was ultimately set by the maximum pressure buildup allowable in the electron gun chamber, viz. 10^{-5} Torr. It was found during calibration that a final orifice diameter of 0.028 inch had to be used in the drift tube for the gun chamber pressure to remain within this limit for test section pressures up to 2 Torr. This orifice size limited the beam current during calibration to 200 microamps. For shock tunnel runs the gun chamber was isolated from the test section pressure after the useful test period by closing a pneumatically-operated ball valve. This arrangement permitted the use of a larger diameter 0.060 inch for the final orifice in the drift tube, which in turn yielded a beam current of one milliampere for the shock tunnel runs.

To avoid a small ac ripple in the beam current, the filament heater circuit was opened by a trigger from the shock tube just prior to shock tunnel flow in the nozzle. The filament thus operated during the run entirely on thermal inertia. Steadiness of the current during the test time was checked by observing the current after filament shut-off without flow in the nozzle. The current would continue for the four to six millisecond period typical of shock tunnel test time at a steady level within three to five percent of the pre-shut-off level. In addition, the scattered current collected on the interior of the end of the drift tube was monitored during shock tunnel operation and was found to remain steady.

Since the shock-tunnel test section is evacuated to a pressure of a few microns of mercury prior to the test, it was considered important to avoid suction of the boundary layer through the orifice provided for the beam in the nozzle wall. To minimize this potential disturbance in the boundary layer being traversed by the electron beam, a series of relief holes were incorporated in the nozzle wall just downstream from the electron beam orifice. These were designed to allow rapid filling (within one millisecond) of a small, enclosed volume surrounding the path of the beam between the end of the electron beam drift tube and the orifice in the nozzle wall.

The electron beam fluorescence was viewed through a port cut into the nozzle wall such that the edge of the port closest to the beam was approximately nine inches from the beam (or one-eighth of the nozzle circumference). Although this arrangement set the axis of the viewing optics system at 20 degrees away from normal to the beam, it was adopted to avoid possible disturbances in the instrumented region of the wall and of the boundary layer. The option of using a viewing system with an axis normal to the beam, but looking upstream, was discarded because of potential errors which could be produced by radiation from the hot gas in the nozzle throat or from the shock system which would have formed over the viewing optics hardware.

The image of the electron beam fluorescence was formed at a distance of 39 inches from the beam with a one-to-one optical system using a pair of 3.1-inch diameter f/6.3, coated, achromatic lenses. The luminescence at points along the beam image was picked up by fiber optics (light guide) bundles and transmitted through them to conventional photomultipliers. Six points close to the nozzle wall (within 1.2 inches) were viewed with fiber optics bundles six inches in length and having a rectangular end at the beam image 0.1 inch along the beam and 0.125 inch across the beam. Seven additional points over the range 1.8 to 5.85 inches from the wall were viewed with one-foot long bundles having a rectangular cross section 0.1 inch (along the beam) by 0.475 inch. The fiber optics bundles, supplied by American Optical, were circular at the end connected to the photomultipliers. Glass filters (Corning No. 5-58), having peak transmission at 4100 Å and dropping to ten percent of peak transmission at 3600 and 4600 Å, were placed between the light guide ends and the photomultiplier cathode to select radiation primarily from the 0,0 and 0,1 bands of the N_2+ first negative system (with band heads centered at 3914 and 4278 Å, respectively).[32] The peak spectral response of the photomultiplier units (Dumont 6467 with an S11 cathode) occurs at 4400 Å. The fiber optics bundles are known to have reduced transmittance in the blue region of the spectrum (dropping sharply for wavelengths below 4000 Å), but the units used were not specifically calibrated to measure the transmission efficiency. It is simply assumed that the effect is consistent independent of possible temperature effects on the intensity distribution within each of the bands and is therefore adequately incorporated in the beam calibration, especially since the temperatures encountered in the test program were comparable to the calibration temperature.

3. Beam Calibration

The use of electron-beam-induced luminescence to infer gas density requires that the relationship between total received light, beam current, and density be known. In its present application the entire electron beam system, including viewing optics, was calibrated with dry air as the test gas over the range 0.18 (Torr) to 2.15 Torr at room temperature (0.55 to 6.6 x 10^{-6} slugs/ft^3 in density). The accelerating potential for the electron beam was held constant at 40 kV.

Collection of the beam current presented something of a challenge. Although the portion of the beam intended for use was the segment within six inches of the shock tunnel nozzle wall, earlier experience with the electron beam system had shown that the glow around a current collection cup could interfere with the measurement of beam luminescence at points along the beam which are too close to the current cup. Consequently, in the present program -- both for calibration and during the shock tunnel runs -- the current collection cup was located at 13.65 inches from the nozzle wall, near the axis of the nozzle. The cup, sketched in Figure 2, was made from graphite stock. To take into account the spreading of the electron beam encountered in the density range of the present program, a device was installed in the tunnel during calibration to permit a current cup to be extended to intercept the beam at the wall (close to the orifice in the nozzle wall) and then to be retracted to permit measurement of the current collected by the remote current cup. In this way a calibration of the total beam current and of the current scattered outside the remote, one-inch diameter cup could be made as a function of the gas density, as shown in Figure 16.

In the actual shock tunnel runs the test section was evacuated prior to the run to a pressure of less than 5 microns of mercury. In this case the beam spreading is negligible, and the total beam current is collected by the remote collection cup. During the shock tunnel run the beam traverses gas at the freestream core density over most of its path and, therefore, spreads such that a smaller, but steady, current is collected during the run. The ratio of the current collected during the run to the pre-flow current is also shown in Figure 16 as a function of the gas density in the freestream core. It can be seen that the current loss is somewhat greater in the flowing case despite the fact that, for the present test conditions, the gas densities in the boundary layer were lower than the density in the nozzle core. The effect of density changes is seen to produce similar changes in collected current for both the static calibration and the measurements with gas flow. In the present experiments the primary current measurement during static calibration was made by using the remote one-inch cup (at 13.65 inches from the wall). At each level of air density in the static calibration the output voltage of the photomultiplier for each viewing channel was normalized by the total beam current inferred from the measured cup current and Figure 16.

The lower curve was used because it yielded better agreement between the density calibration curve (Figure 17) and the absolute value of freestream density during the tests. The relative variation in density across the boundary layer is unaffected by the choice of curves from Figure 16, since the two curves are in a constant ratio.

Figure 17 is a typical calibration curve for air with one of the two outermost viewing channels. Some nonlinearity is noted over the entire range of the calibration, but not enough to affect resolution of density variations at the upper range.

Although the primary objective of the shock tunnel tests was the observation of the relative variation in density across the boundary layer, it is of interest to note the accuracy of the absolute value of density as inferred from the light received from a point in the freestream. The experimental output for the photomultiplier whose static calibration is shown in Figure 17 was divided by the indicated pre-flow current and entered on Figure 17 at the value of freestream density computed from the measured freestream pitot pressure for each of the shock tunnel runs. The points at densities of approximately 6×10^{-6} slugs/ft^3 lie slightly below the static calibration, while the single point at 3×10^{-6} slugs/ft^3 is slightly higher than the calibration curve. Although the source of the observed differences is not known, beam spreading, as considered in the following discussion, is not believed to be responsible.

4. Beam Profiles

A primary concern in applying the electron beam to the measurement of density is that of accounting correctly for the total light generated at a given station along the beam and of including the full beam current which produces the beam luminescence. One method of assessing beam characteristics is that of interpreting photographs of the beam luminescence. Photographs taken of the beam at two pressures (0.82 and 1.6 Torr) have been analyzed to determine the distribution of light intensity at several stations along the beam. A print of the photograph taken at 0.85 Torr is included as Figure 15. The spot seen at one end of the beam is associated with the exposed end of the drift tube and apparently results from scattering through the final orifice, which is 0.060 inch in thickness. During shock tunnel runs a cover plate with a relatively large hole (0.15 inch diameter) for the beam was in place, as seen in the configuration photograph, Figure 1, and screened the spot from the view of the optics. The negatives of the two photographs were scanned on a microdensitometer with an effective viewing rectangle 20 microns wide (across the beam) and 0.115 inch long (along the beam) in the actual scale of the experiment. A film calibration of the Royal Pan film with an exposure step table indicated that except for very low exposures the dependence of film density, D, on exposure, E, is $\Delta D = \Delta \log E$. Since exposure is the product of light intensity and time and since the exposure time is constant for a given photograph, the change in film density is therefore equal to the change in the logarithm of the local light intensity.

Several important characteristics of the beam could be inferred from the film scans, samples of which are shown in Figure 18. Light intensity as calculated from film density is shown on the ordinate in Figure 18; the abscissa represents the actual scale of the cylindrical radius from the center of the beam. The decrease in peak intensity and the spreading of the profile along the beam as a result of beam spreading are clearly shown. At each station three beam characteristics were determined:

1) total light (found by integrating the total area under the intensity vs. radial distance plot).
2) integrated light within the width viewed by the fiber optics at each station
3) the half intensity width, $W_{1/2}$ (width at which the light intensity is half the peak intensity at that station).

The results of these measurements are shown in Figure 19. At the top of the figure is shown the ratio of the integrated total light at a given position along the beam to the integrated total light at the wall (actually 0.2 inch from the wall position when the cover plate is in place). Within the reading and integration error, there is not significant attenuation in total light (or total beam current) along the 5 1/2 inches of the beam photographed. The indicated increase in (total light)/(total light at wall) with distance along the beam for the 1.6 Torrcase is unrealistic and is believed to be a result of reading and integration errors involved in reading the photographs. In the lower curves at the top of the figure the fraction of total light found to be within the viewing width of the fiber optics bundles seems alarmingly low because it falls in the range of 50 to 70 percent of the total light. However, closer inspection reveals two important characteristics, viz., that the fraction of light viewed changes little with either distance along the beam or pressure (density) level, both of which should have an effect on spreading the beam. It should be noted here that the photographs from which these measurements were made were obtained with an unfiltered system, that is, with a conventional camera viewing the beam through a clear glass plate. Radiation from systems other than the N_2^+ first negative may therefore have been included in the photograph although excluded in the actual filtered optics system used in calibration and test. For example, there exists some evidence[33] that excitation and radiation of neutral N_2 molecule is mainly produced by low-energy secondary electrons and might, therefore, produce a wider profile than the N_2 radiation. The test data were therefore reduced without any attempt to account for "missed light" in either calibration or test. This approach seems to be validated by the fact that the boundary layer density determined in this way shows no step change at the adjacent points in the boundary layer (at 1.3 inches from the wall) viewed by adjacent optics channels with viewing widths of 0.125 inch and 0.475 inch, respectively.

Finally, Figure 19 also presents the readings of the half-intensity widths as a function of distance along the beam. The fiber optics widths are shown by solid lines. It is interesting to note that the beam remains effectively focused for the first inch or two after it passes through the nozzle wall, then begins to spread rapidly. Probably more by coincidence than by actual duplication, the beam spreading in the outer portion of the beam follows very well the empirical correlation of beam spreading reported by Camac.[33] The effect of gas density on beam spreading seems to be slightly greater in the present measurements, however, than in the Camac correlation. The primary core of the beam is seen to remain well within the width of the viewing optics, with the possible exception of the outermost point at the 1.6 Torr condition. The beam calibrations and shock tunnel readings have been used directly without attempts to account for the apparently small relative differences in beam spreading between the calibration (at constant density) and the shock tunnel run (with density variations in the boundary layer thickness of just less than six inches and with constant density over the remaining path to the current collection cup).

The spectral distribution of the beam luminescence from the N_2^+ first negative system is a function of the vibrational temperature of the gas at elevated temperatures. Thus a possible discrepancy can arise if the calibration is made at room temperature and the test made at a higher gas temperature. In the present case, however, the maximum static temperature in the boundary layer is approximately $1000^{\circ}R$. Even if the vibrational excitation level freezes in the nozzle expansion, the maximum vibrational temperature would be approximately $1500^{\circ}R$, which is well below the range at which the N_2^+ first negative band intensities are affected to a detectable degree by the vibrational temperature of the gas.

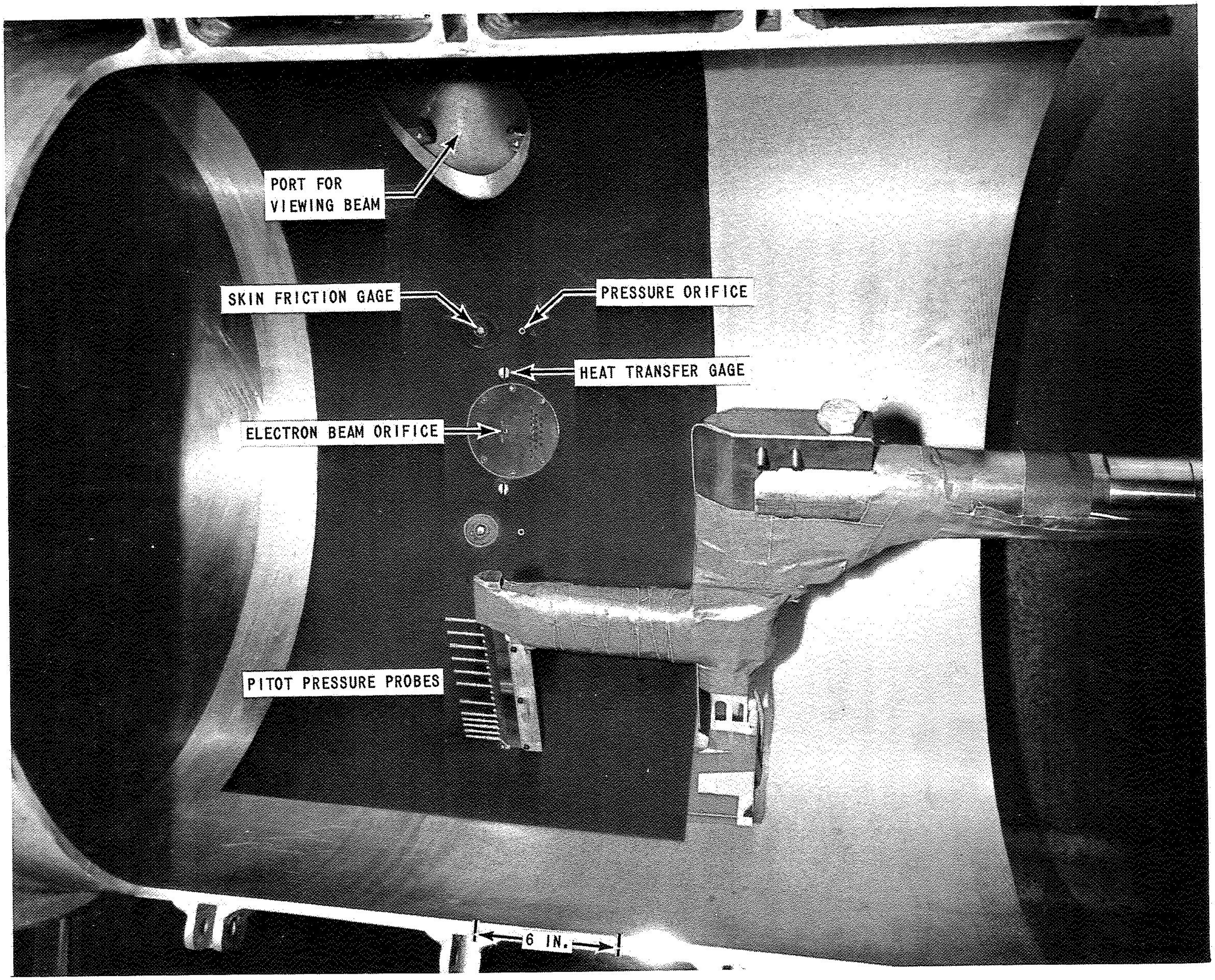

Figure 1 NOZZLE INSTRUMENTATION FOR TURBULENT BOUNDARY LAYER EXPERIMENTS

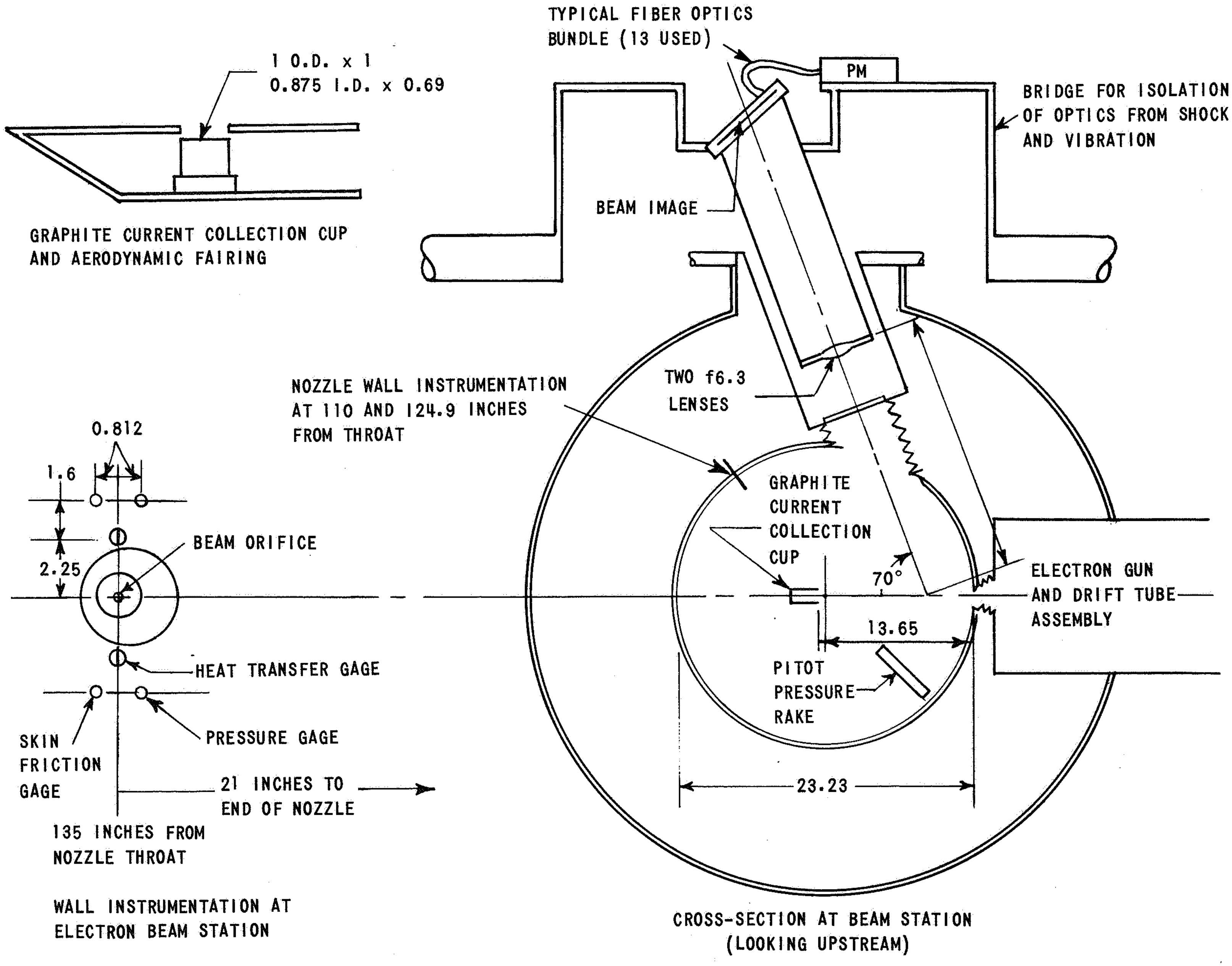

Figure 2 NOZZLE INSTRUMENTATION AND VIEWING OPTICS (NOT TO SCALE - ALL DIMENSIONS IN INCHES)

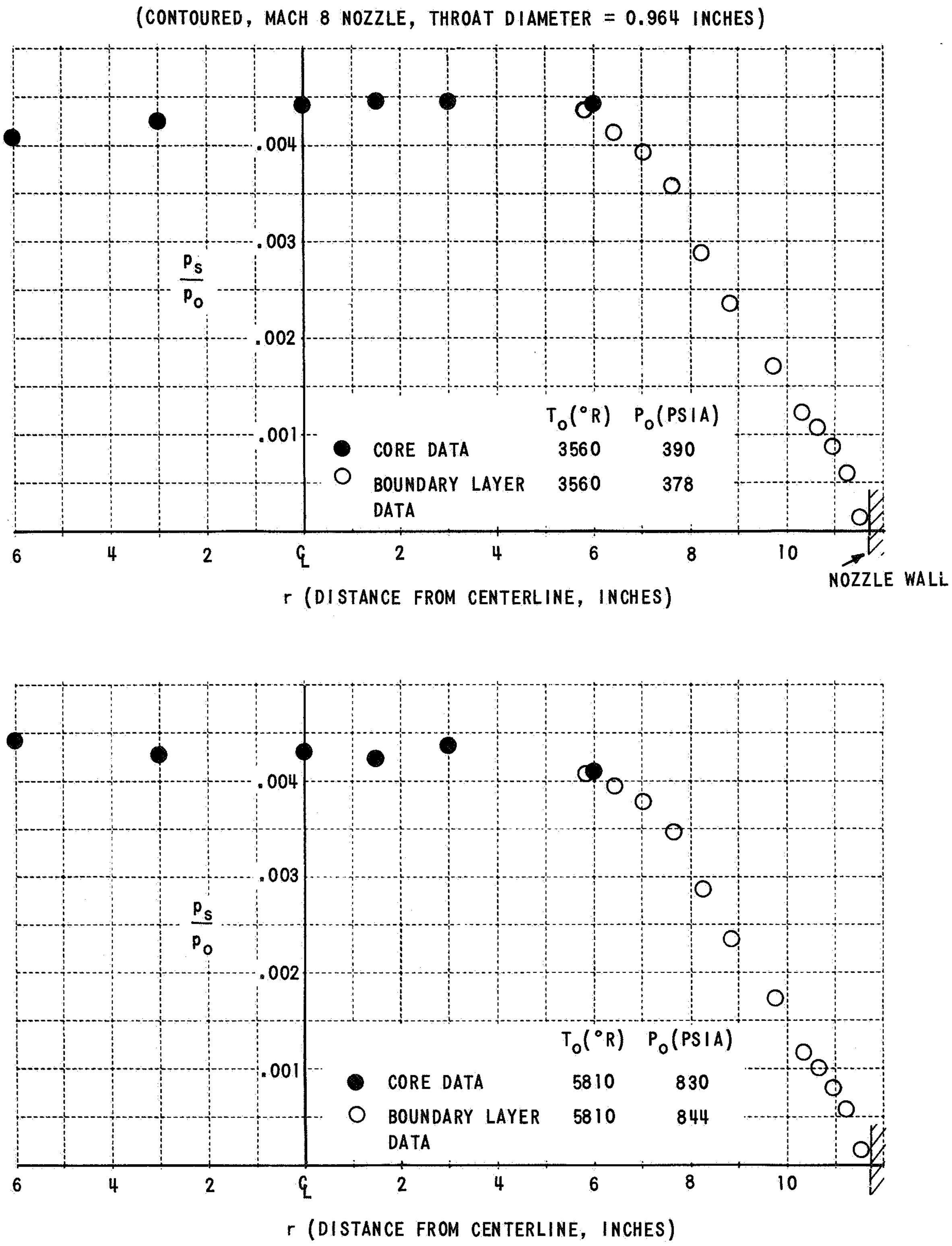

Figure 3 NOZZLE PITOT PRESSURE DISTRIBUTIONS

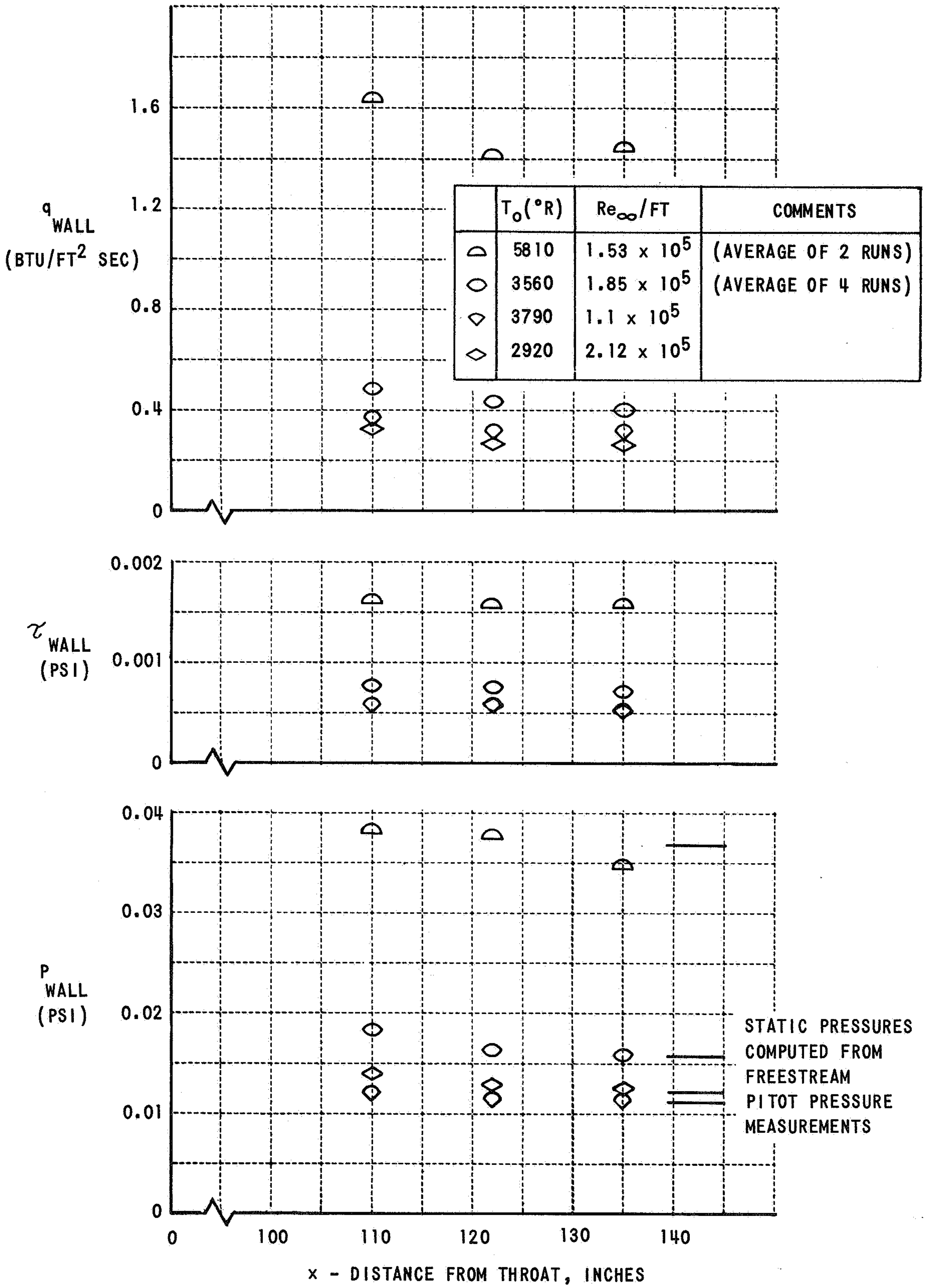

Figure 4 EXPERIMENTAL DATA ON THE NOZZLE WALL

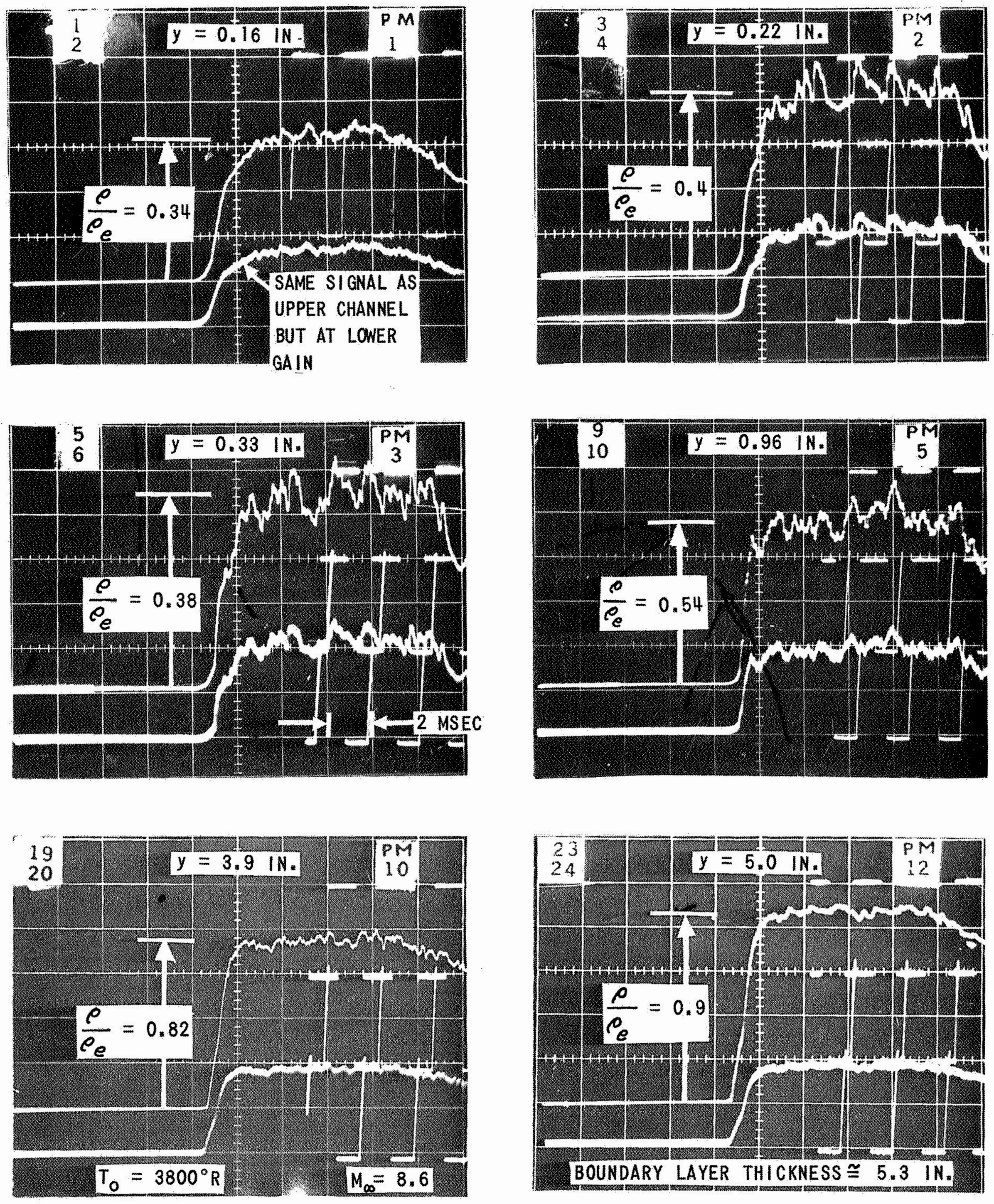

Figure 5 PHOTOMULTIPLIER RECORDS FROM ELECTRON BEAM LUMINESCENCE IN A TURBULENT BOUNDARY LAYER

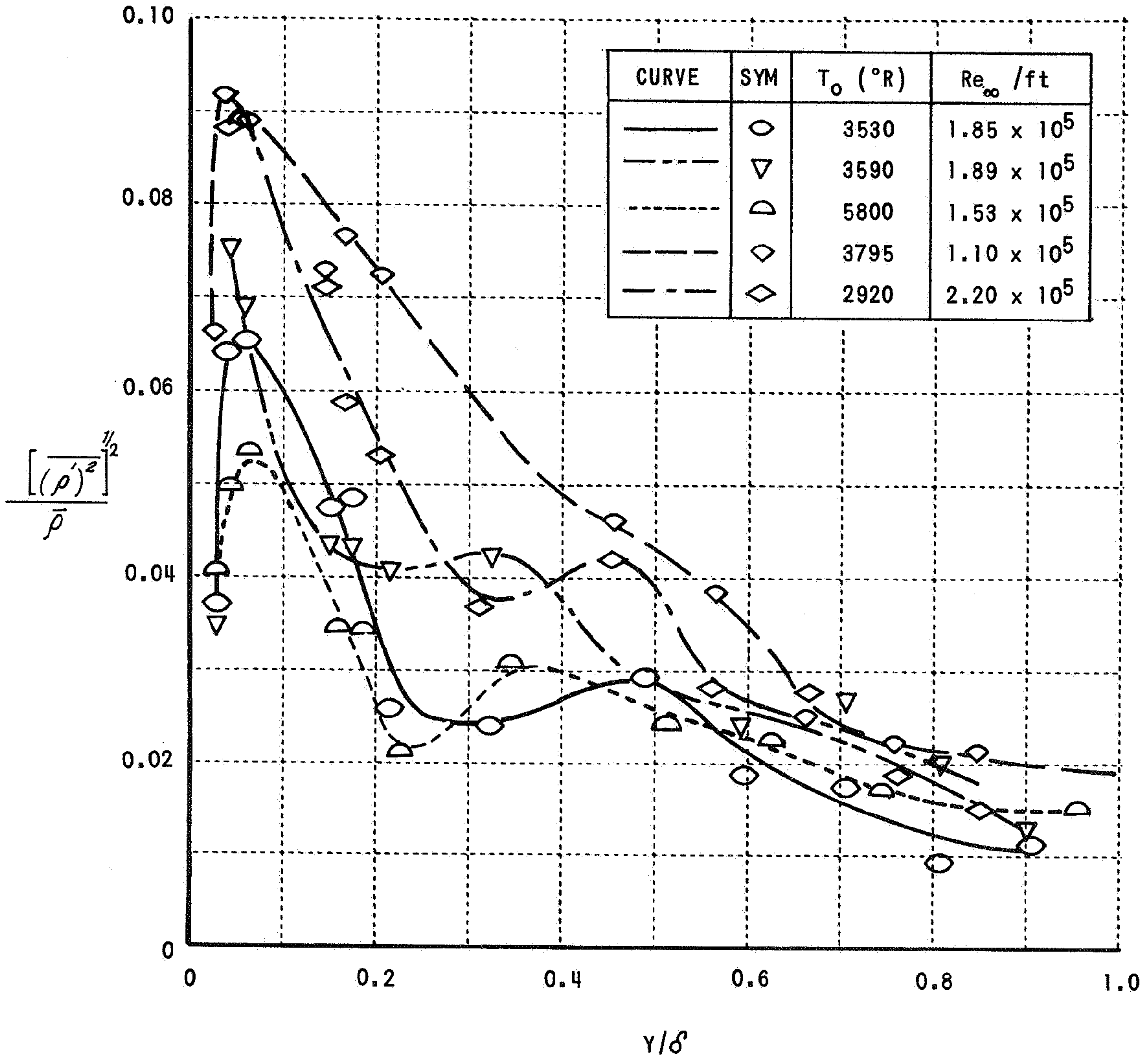

Figure 6 INTENSITY OF DENSITY FLUCTUATIONS FROM PHOTOMULTIPLIER RECORDS

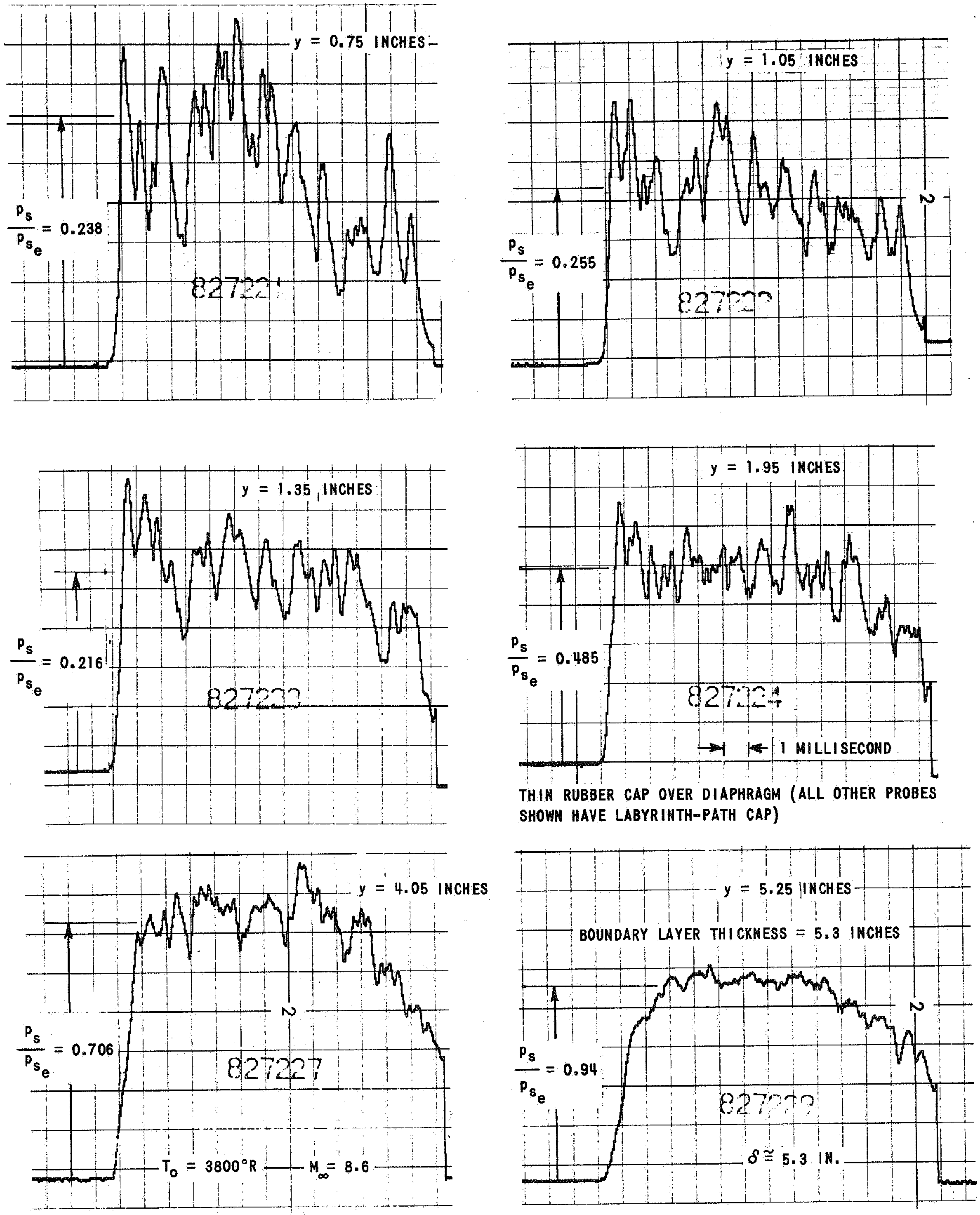

THIN RUBBER CAP OVER DIAPHRAGM (ALL OTHER PROBES SHOWN HAVE LABYRINTH-PATH CAP)

Figure 7 RECORDS OF PITOT PRESSURE IN A TURBULENT BOUNDARY LAYER

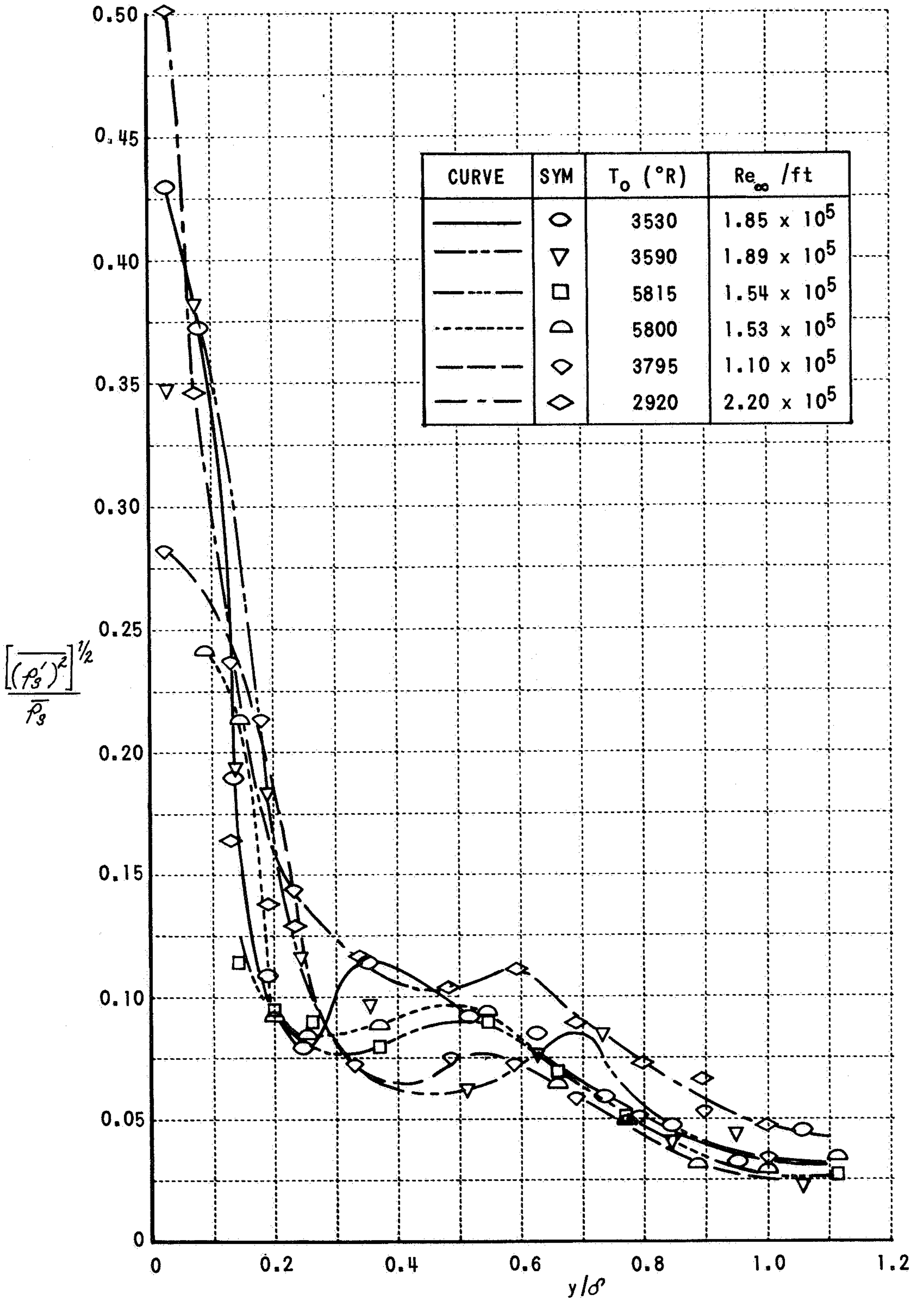

Figure 8 INTENSITY OF PITOT PRESSURE FLUCTUATIONS

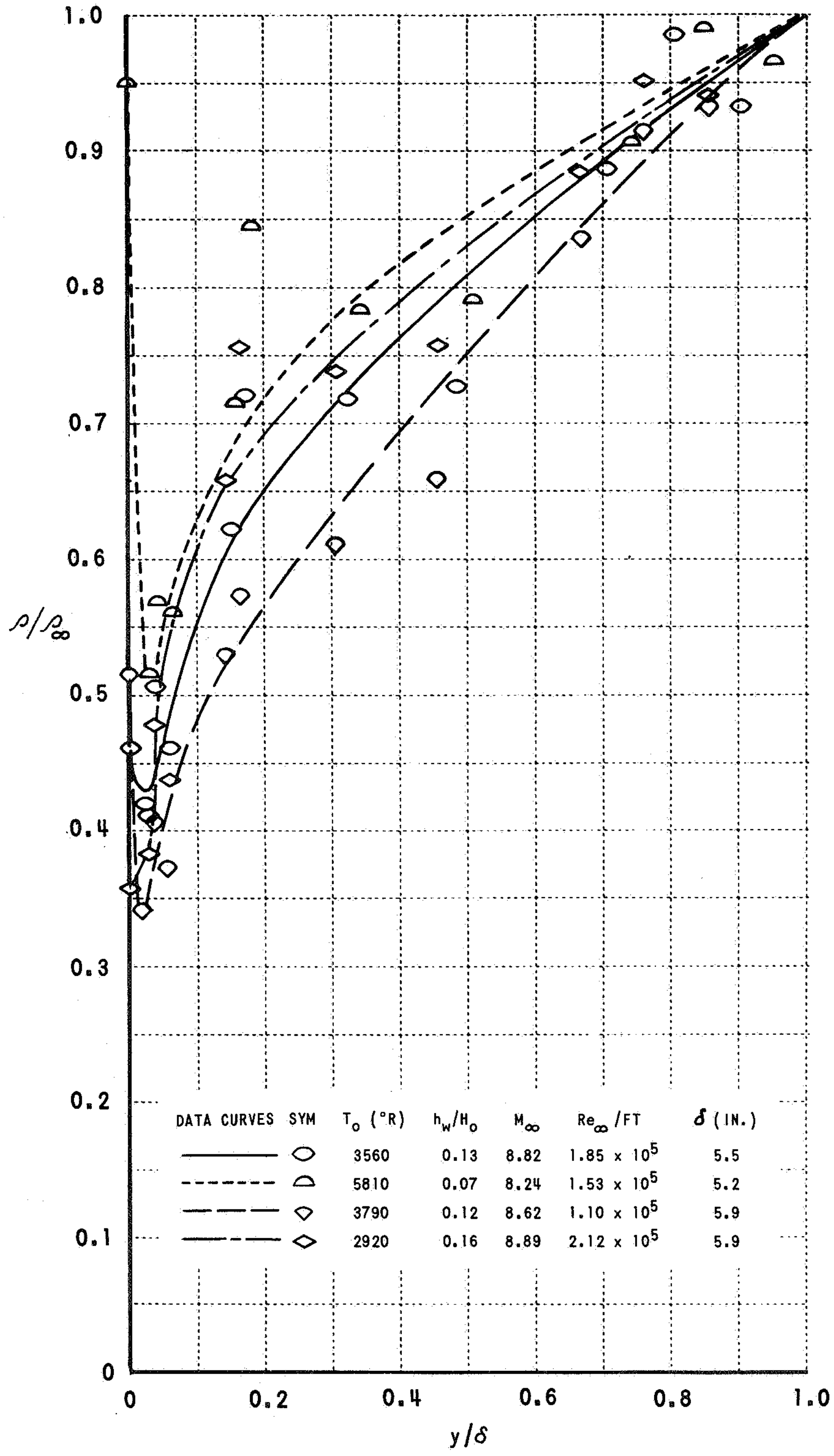

Figure 9 MEASURED DENSITY PROFILES

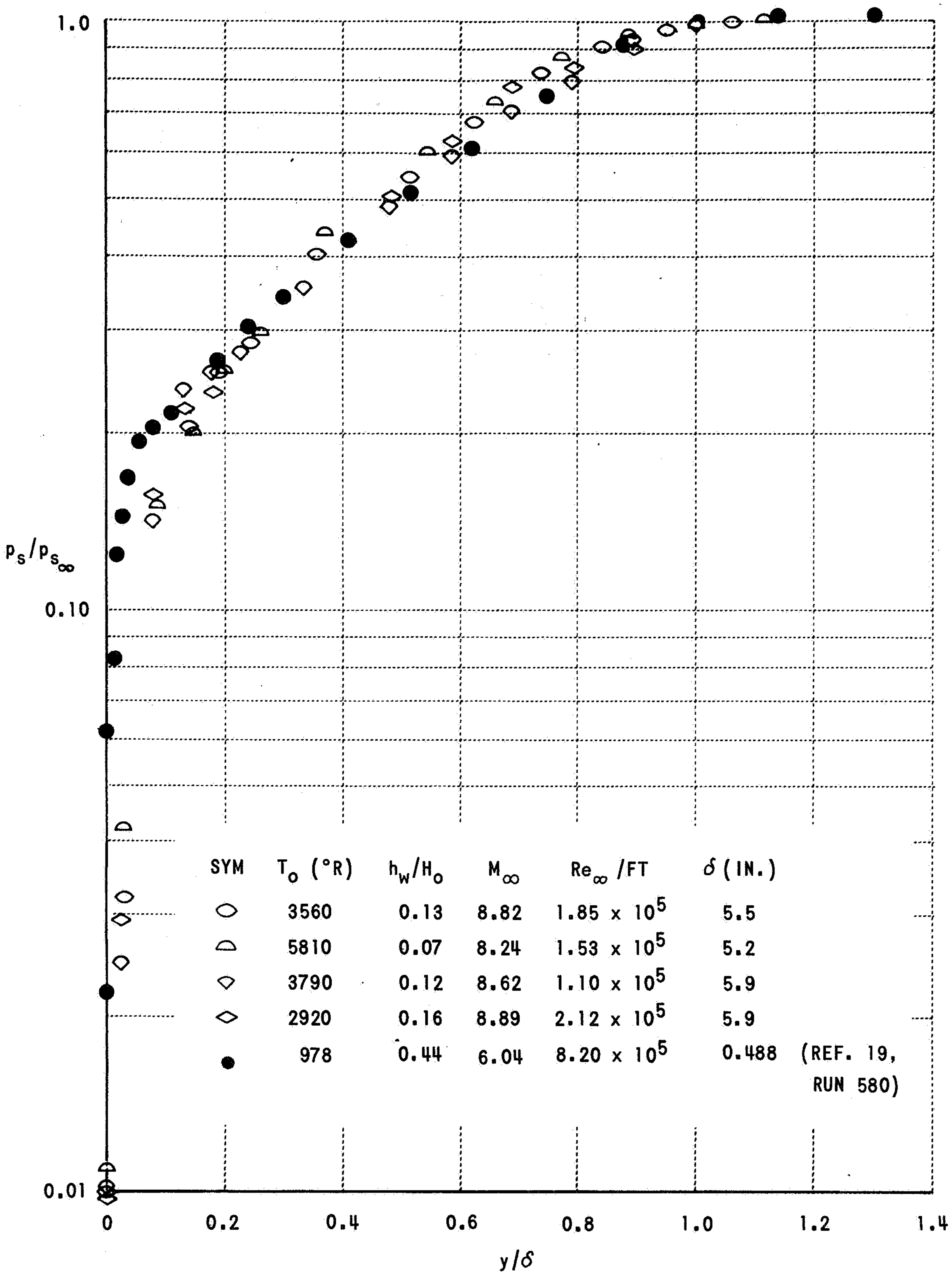

Figure 10 MEASURED PITOT PRESSURE PROFILES

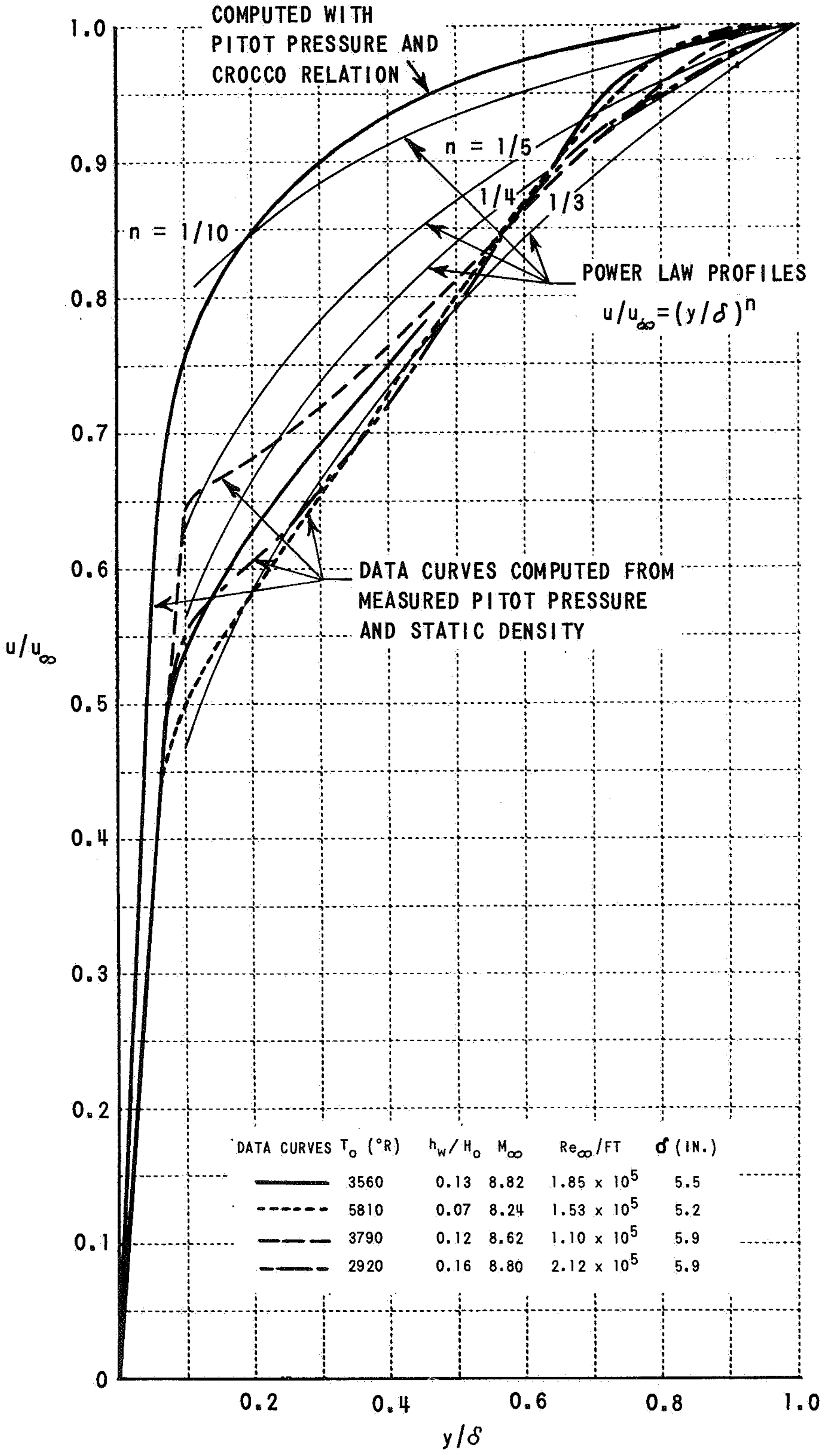

Figure 11 COMPARISON OF COMPUTED EXPERIMENTAL VELOCITY PROFILES WITH POWER LAW PROFILES

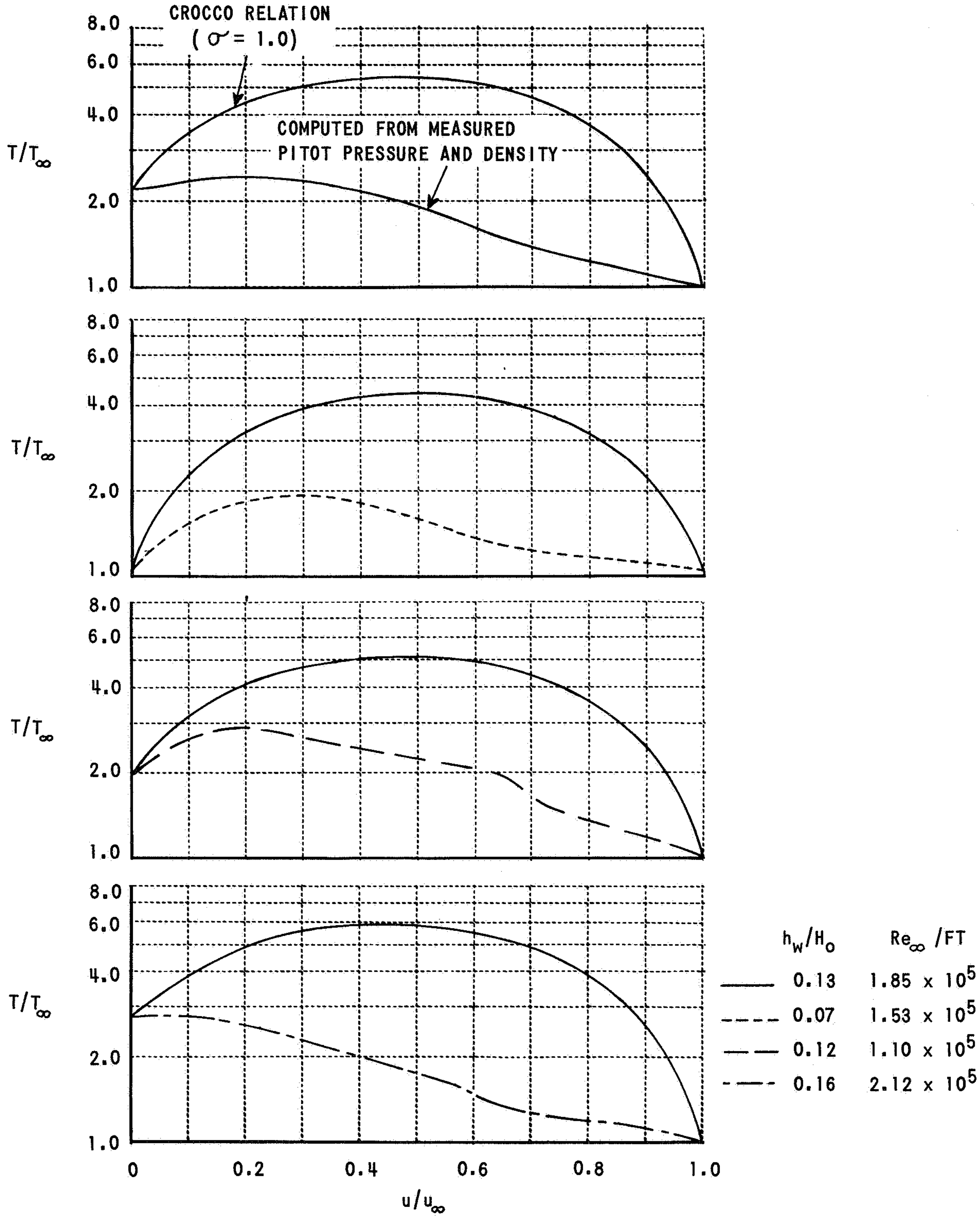

Figure 12 COMPARISON OF EXPERIMENTAL TEMPERATURE PROFILES WITH CROCCO THEORY

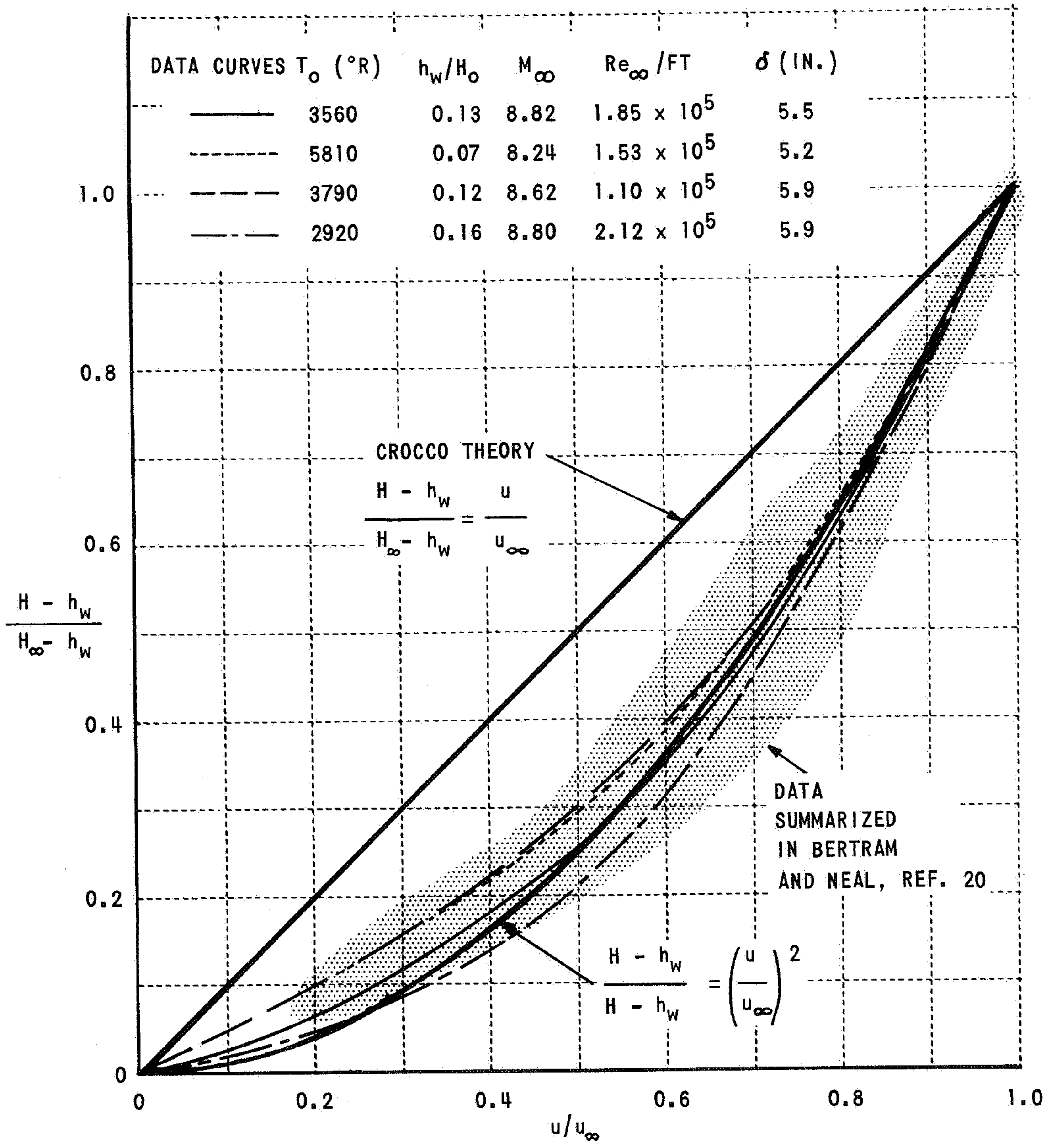

Figure 13 COMPARISON OF TOTAL ENTHALPY PROFILE WITH CROCCO THEORY

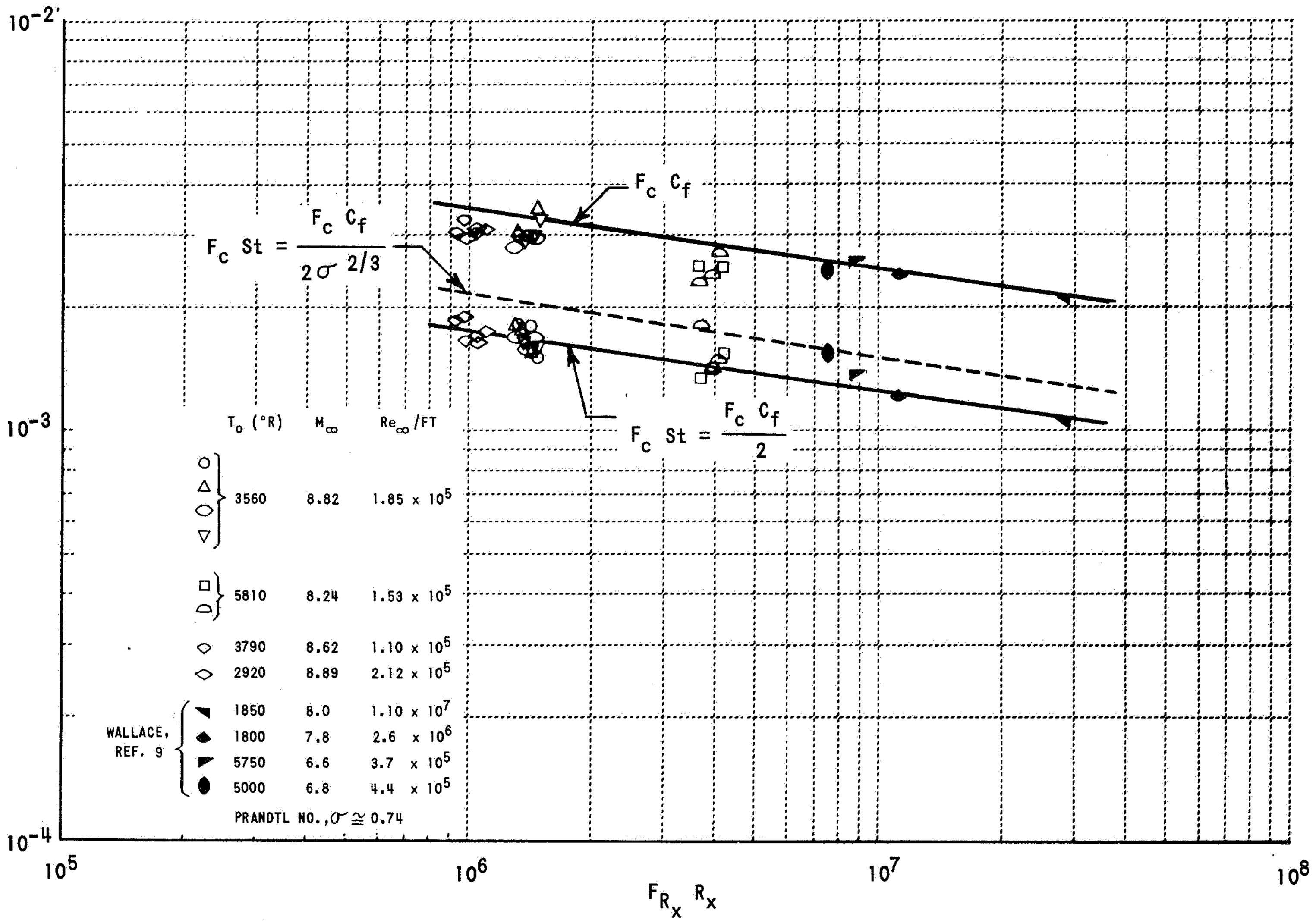

Figure 14 COMPARISON OF TURBULENT BOUNDARY LAYER SKIN FRICTION AND HEAT TRANSFER WITH SPALDING AND CHI THEORY

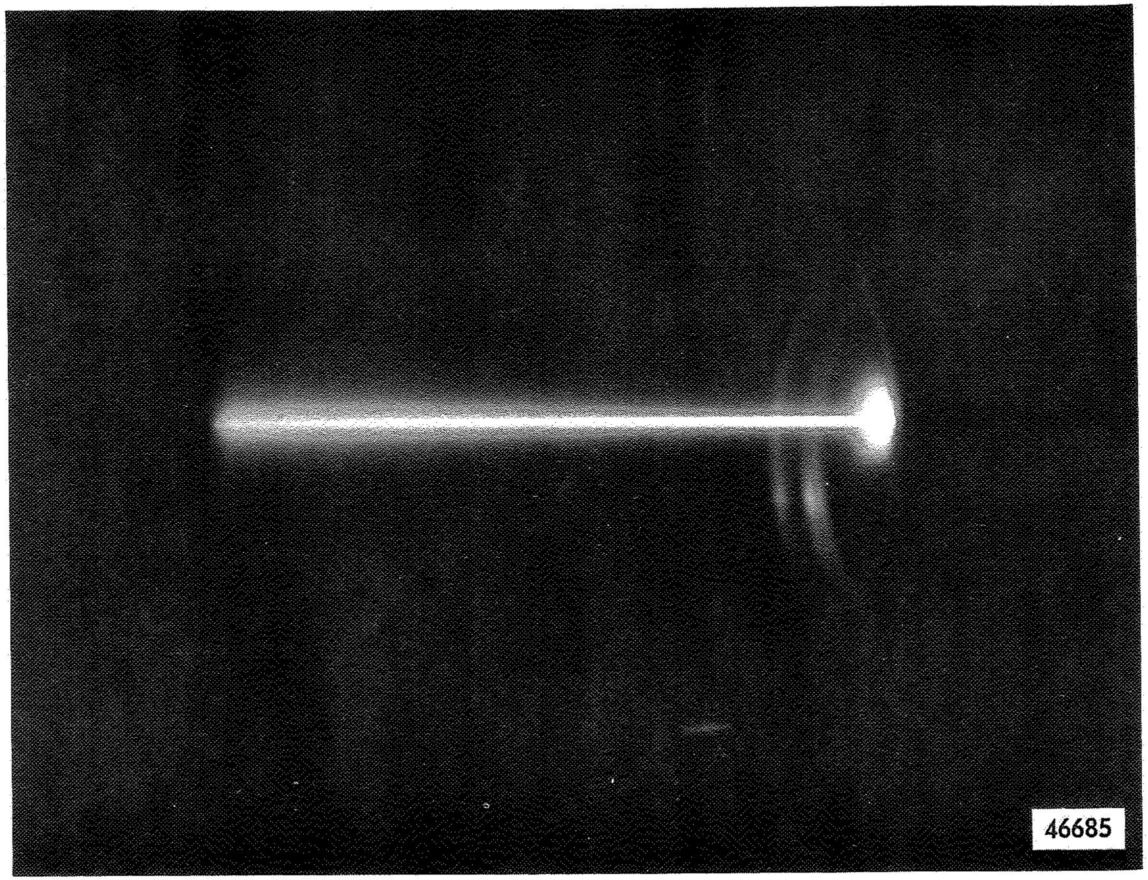

Figure 15 ELECTRON BEAM IN SHOCK-TUNNEL NOZZLE CONFIGURATION
(BEAM LENGTH 6 INCHES, PRESSURE = 0.85 Torr)

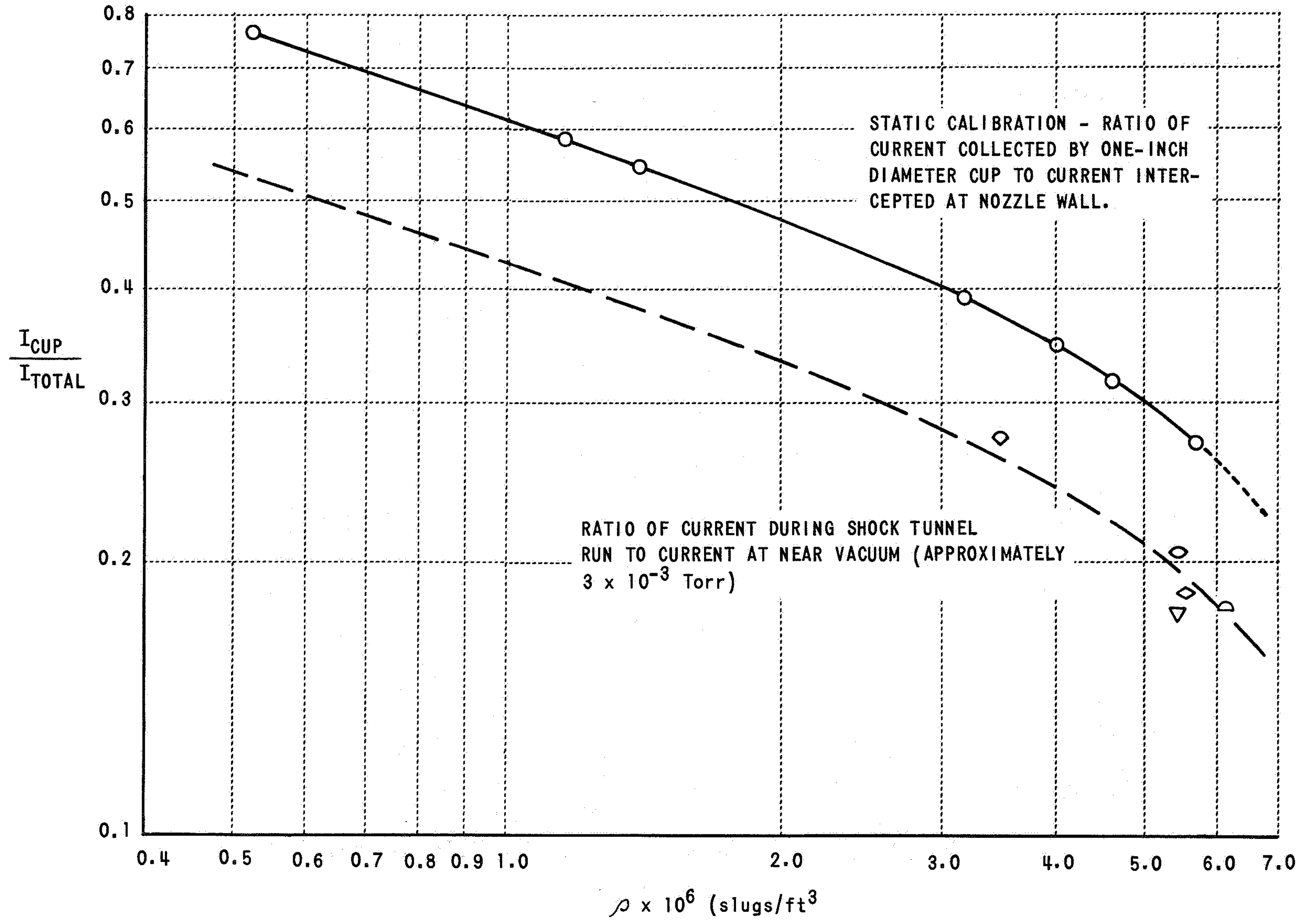

Figure 16 EFFECT OF BEAM SPREADING ON CURRENT COLLECTION

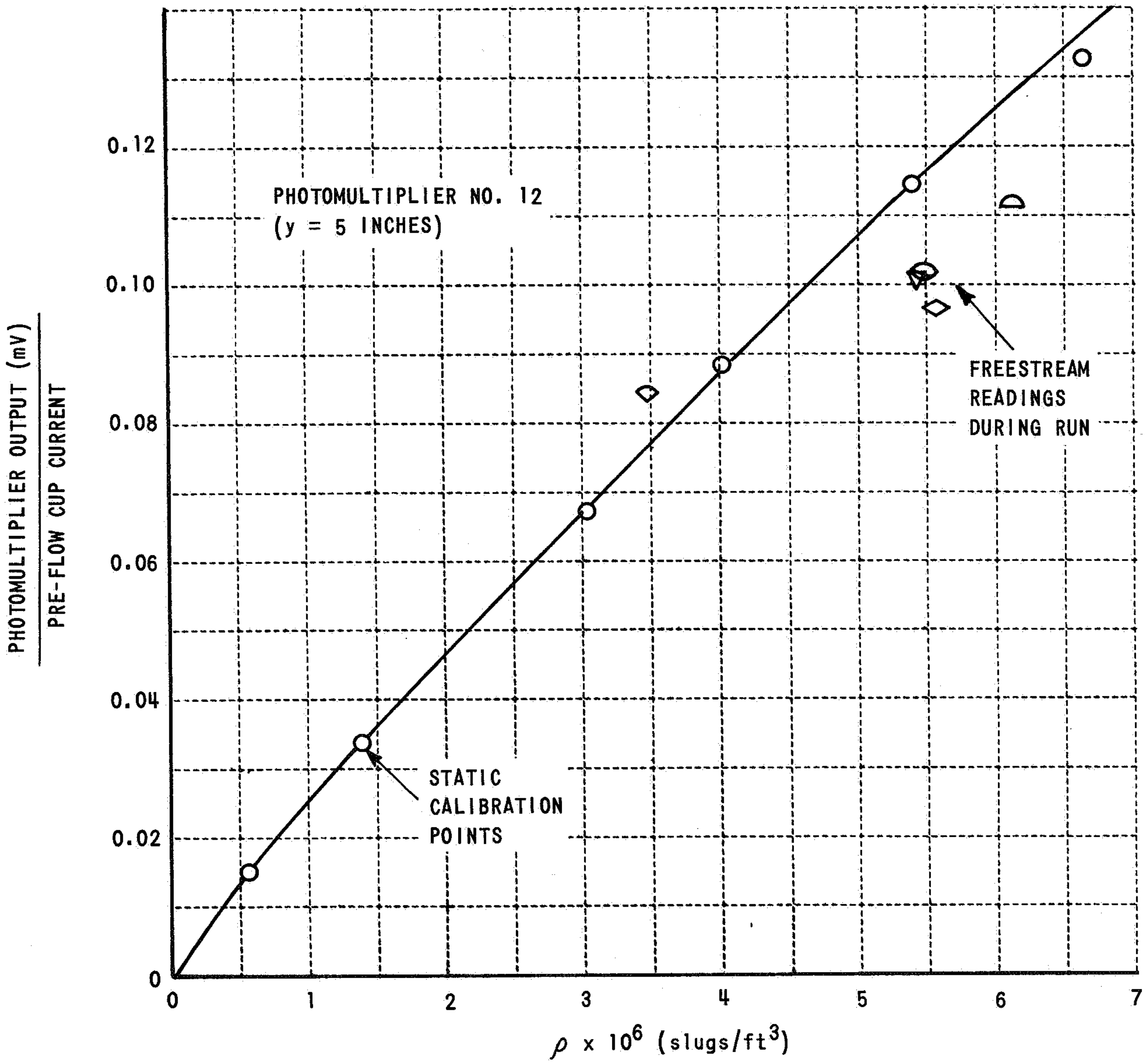

Figure 17 DENSITY CALIBRATION CURVE

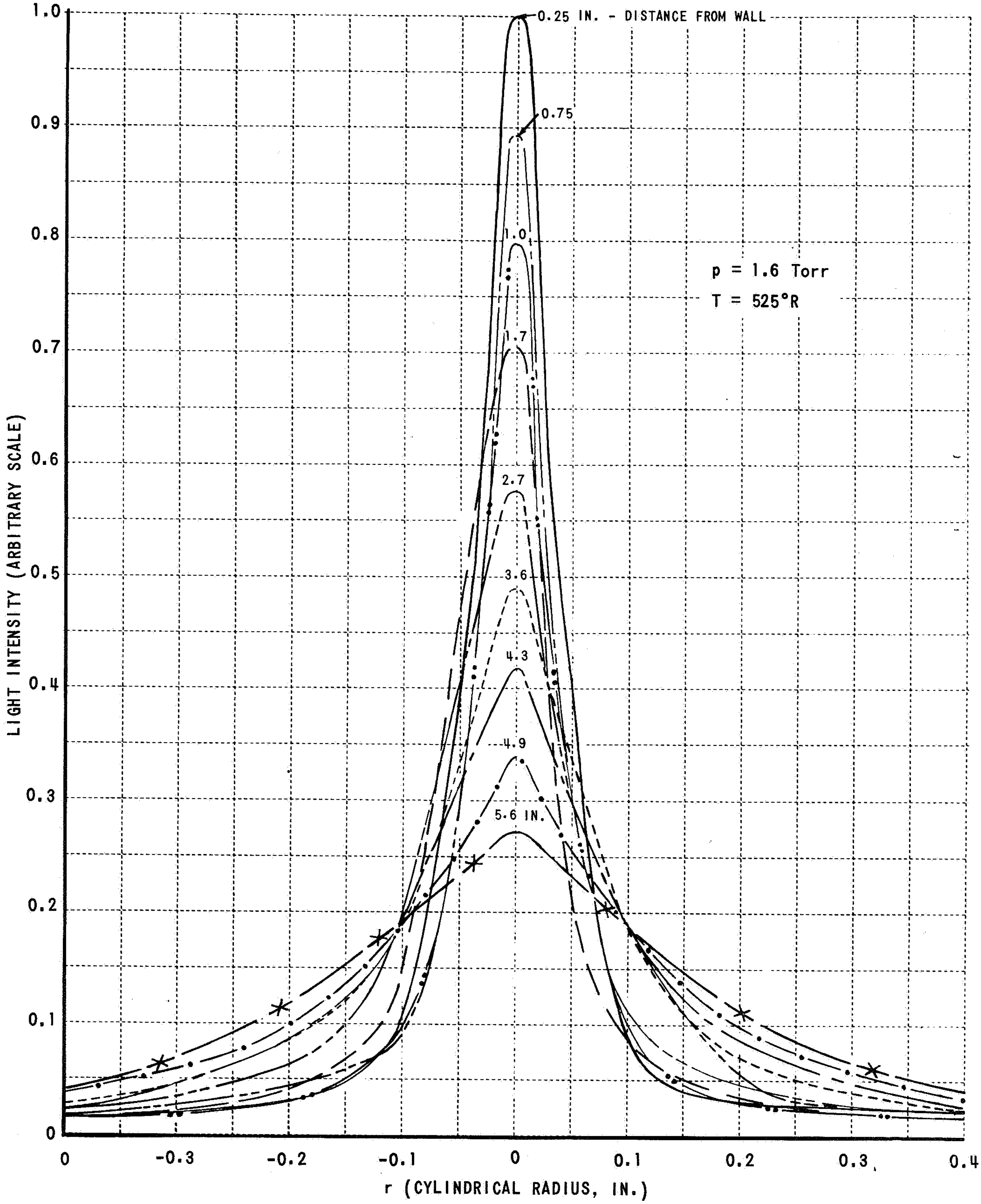

Figure 18 ELECTRON BEAM LUMINESCENCE PROFILES CALCULATED FROM DENSITOMETER READINGS OF BEAM PHOTOGRAPH

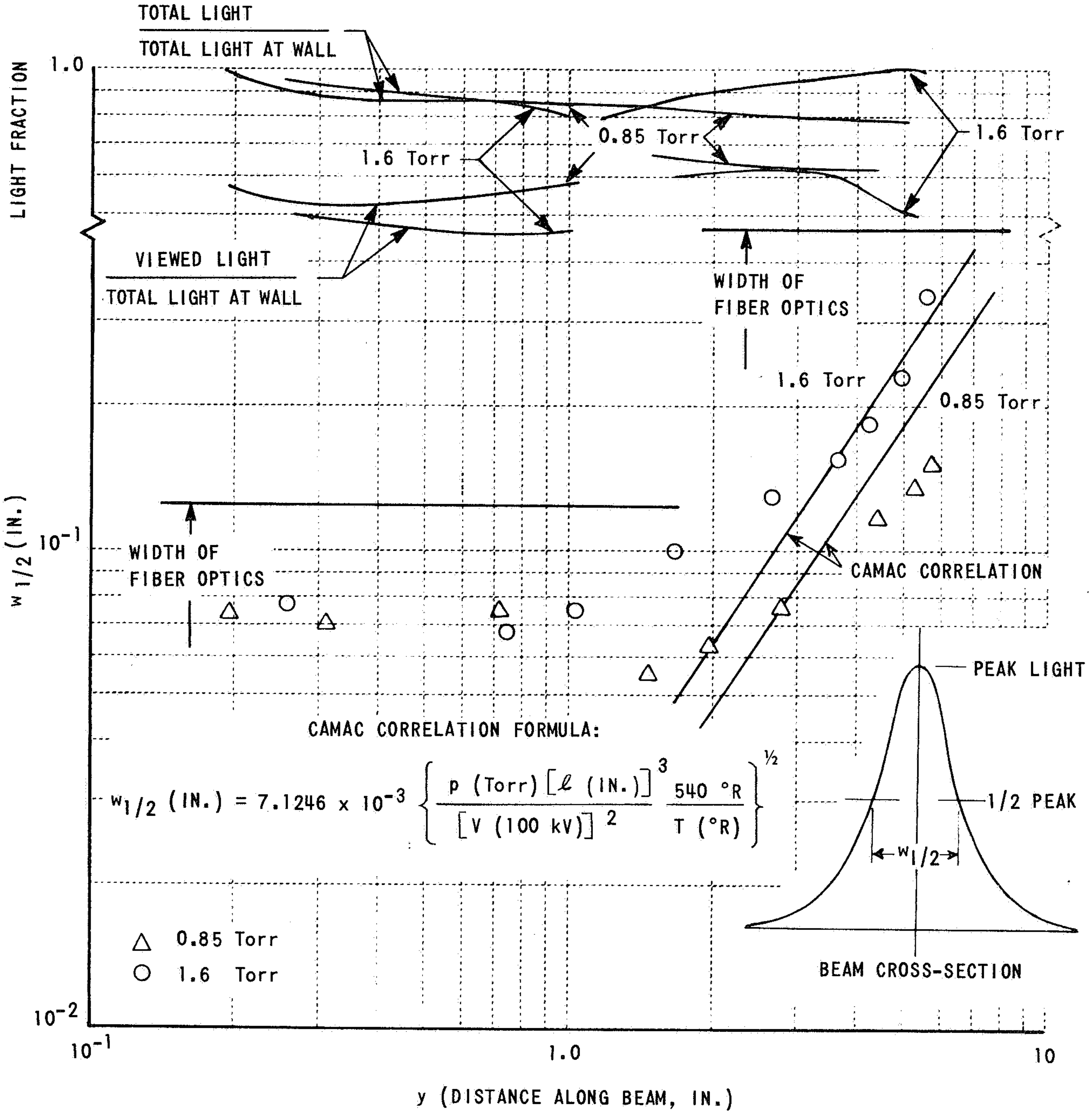

CAMAC CORRELATION FORMULA:

$$w_{1/2}\ (\mathrm{IN.}) = 7.1246 \times 10^{-3} \left\{ \frac{p\ (\mathrm{Torr})\,[\ell\ (\mathrm{IN.})]^{3}}{[V\ (100\ \mathrm{kV})]^{2}}\ \frac{540\ ^{\circ}\mathrm{R}}{T\ (^{\circ}\mathrm{R})} \right\}^{1/2}$$

Figure 19 ELECTRON BEAM CHARACTERISTICS FROM DENSITOMETER READINGS OF BEAM PHOTOGRAPHS